

AN EDDINGTON LIMITED ACCRETION DISK WIND IN THE NARROW LINE SEYFERT 1, PG 1448+273.

J. N. REEVES^{1,2}, V. BRAITO^{1,2,3}, A. LUMINARI^{4,5}, D. PORQUET⁶, M. LAURENTI^{7,8}, G. MATZEU⁹, A. LOBBAN¹⁰, S. HAGEN¹¹

(Received)

Draft version August 28, 2024

ABSTRACT

PG 1448+273 is a luminous, nearby ($z = 0.0645$), narrow line Seyfert 1 galaxy, which likely accretes close to the Eddington limit. Previous X-ray observations of PG 1448+273 with *XMM-Newton* in 2017 and *NuSTAR* in 2022 revealed the presence of an ultra fast outflow, as seen through its blueshifted iron K absorption profile, where the outflow velocity appeared to vary in the range $0.1 - 0.3c$. In this work, new X-ray observations of PG 1448+273 are presented, in the form of four simultaneous *XMM-Newton* and *NuSTAR* observations performed in July and August 2023. The X-ray spectra appeared at a similar flux in each observation, making it possible to analyze the mean 2023 X-ray spectrum at high signal to noise. A broad ($\sigma = 1$ keV) and highly blue-shifted ($E = 9.8 \pm 0.4$ keV) iron K absorption profile is revealed in the mean spectrum. The profile can be modeled by a fast, geometrically thick accretion disk wind, which reveals a maximum terminal velocity of $v_\infty = -0.43 \pm 0.03c$, one of the fastest known winds in a nearby AGN. As a result, the inferred mass outflow rate of the wind may reach a significant fraction of the Eddington accretion rate.

Subject headings: galaxies: active — quasars: individual (PG 1448+273) — X-rays: galaxies — black hole physics

1. INTRODUCTION

Since their initial discovery two decades ago (Chartas et al. 2002; Pounds et al. 2003; Reeves et al. 2003), ultra fast outflows (or UFOs) in X-rays have been found to occur in about 40% of Active Galactic Nuclei (Tombesi et al. 2010). Most of these detections arise through studies of the iron K band towards nearby and X-ray bright, local ($z < 0.1$) Seyfert 1 AGN, with typical outflows velocities of around $0.1c$; e.g. Tombesi et al. 2010; Gofford et al. 2013; Igo et al. 2020; Matzeu et al. 2023. The mechanical power of these winds can typically reach up to a few percent of the Eddington limit (Tombesi et al. 2013; Gofford et al. 2015), sufficient to provide significant mechanical feedback into the AGN host galaxy (Silk & Rees 1998; Fabian 1999; Di Matteo et al.

2005; King 2003; Hopkins & Elvis 2010). Powerful black hole winds may also play a crucial part in the regulating the growth of super massive black holes in more luminous quasars (Nardini et al. 2015; Tombesi et al. 2015; Matzeu et al. 2023) and notably at high redshifts near the peak of the QSO evolution (e.g. Chartas et al. 2021 and references therein).

At lower redshifts, the Narrow Line Seyfert 1s (NLS1s, Osterbrock & Pogge 1985) represent a part of the AGN population with relatively low black hole masses, yet with high accretion rates with respect to the Eddington limit (Boroson 2002). As such they provide an excellent laboratory for studying accretion disk winds, which produce the observed ultra fast outflows (Proga & Kallman 2004; Sim et al. 2008, 2010a; Fukumura et al. 2010; Mizumoto et al. 2021). Several notable examples of ultra fast outflows have been detected in nearby NLS1s (Pounds & Vaughan 2012; Longinotti et al. 2015; Hagino et al. 2016; Parker et al. 2017; Kosec et al. 2018; Reeves & Braito 2019), expanding the parameter space of AGN accretion disk winds into the high accretion rate regime.

The subject of this paper is the nearby ($z = 0.0645$) NLS1, PG 1448+273, which also shows evidence for a powerful UFO, observed both in the iron K band and at soft X-rays (Kosec et al. 2020; Laurenti et al. 2021; Reeves et al. 2023). It is also classed as a radio-quiet QSO (Schmidt & Green 1983) and has narrow permitted lines, e.g. $H\beta$ FWHM of 1330 km s^{-1} (Grupe et al. 2004), with a bolometric luminosity estimated to be $L_{\text{bol}} = 2 - 3 \times 10^{45} \text{ erg s}^{-1}$ (e.g., Grupe et al. 2004; Rakshit, Stalin & Kotilainen 2020). Recently, a black hole mass estimate of $M_{\text{BH}} = 1.01_{-0.23}^{+0.38} \times 10^7 M_\odot$ was derived by Hu et al. (2021), obtained from a $H\beta$ based reverberation study of 15 PG quasars. Given its observed bolometric luminosity, this implies that PG 1448+273

¹ Department of Physics, Institute for Astrophysics and Computational Sciences, The Catholic University of America, Washington, DC 20064, USA, email reevesjn@cua.edu

² INAF, Osservatorio Astronomico di Brera, Via Bianchi 46 I-23807 Merate (LC), Italy

³ Dipartimento di Fisica, Università di Trento, Via Sommarive 14, Trento 38123, Italy.

⁴ INAF - IAPS, via del Fosso del Cavaliere 100, 00100 Roma

⁵ INAF-Osservatorio Astronomico di Roma, Via Frascati 33, 00078 Monteporzio, Italy

⁶ Aix-Marseille Univ., CNRS, CNES, LAM, Marseille, France

⁷ Dipartimento di Fisica, Università di Roma “Tor Vergata”, Via della Ricerca Scientifica 1, 00133 Roma, Italy

⁸ Space Science Data Center, SSDC, ASI, Via del Politecnico snc, 00133 Roma, Italy

⁹ Quasar Science Resources SL for ESA, European Space Astronomy Centre (ESAC), Science Operations Department, 28692, Villanueva de la Cañada, Madrid, Spain

¹⁰ European Space Astronomy Centre (ESA/ESAC), E-28691 Villanueva de la Cañada, Madrid, Spain

¹¹ Centre for Extragalactic Astronomy, Department of Physics, University of Durham, South Road, Durham DH1 3LE, UK

is likely to accrete near the Eddington limit, which may provide favorable conditions for launching an accretion disk wind, as discussed by Giustini & Proga (2019).

The detection of a fast wind in PG 1448+273 was initially obtained by Kosec et al. (2020) and Laurenti et al. (2021) (see their Figures 3 and 1 respectively), on the basis of a 75 ks *XMM-Newton* exposure in 2017. This 2017 *XMM-Newton* observation occurred just prior to a pronounced dip as observed by the *Swift* monitoring (Laurenti et al. 2021), resulting in an historically low X-ray flux for PG 1448+273. An Fe K absorption trough was measured centered at 7.5 keV, which implied an outflow velocity of $\sim 0.1c$, assuming an identification with the $1s \rightarrow 2p$ resonance lines from He-like (Fe XXV) and H-like (Fe XXVI) iron. It has one of the deepest absorption profiles amongst the UFOs reported to date (c.f. Tombesi et al. 2010; Gofford et al. 2013), with an equivalent width of $EW = -410 \pm 80$ eV. As was inferred by Kosec et al. (2020) and Laurenti et al. (2021), the high equivalent width implies an absorption column density of the order $N_{\text{H}} = 10^{24} \text{ cm}^{-2}$. In particular, the whole absorption profile studied by Laurenti et al. (2021) was modeled with a physically motivated accretion disk wind model; utilizing the WINE (Wind in the Ionised Nuclear Environment) code of Luminari et al. (2018).

The first *NuSTAR* observation of PG 1448+273 (250 ks duration, 125 ks exposure) occurred in January 2022 and revealed strong X-ray variability (Reeves et al. 2023). The first part of the observation (slice A), seen at a much higher flux ($F_{2-10} = 4.8 \times 10^{-12} \text{ erg cm}^{-2} \text{ s}^{-1}$), was coincident with a 70 ks *XMM* exposure and the wind absorption at Fe K had diminished in opacity compared to 2017. During the last 60 ks with *NuSTAR* (slice B), a deep ($> \times 2$) and rapid (< 10 ks) drop in flux was observed and was also accompanied by an increase in spectral hardness. The slice B *NuSTAR* spectrum revealed a deep Fe K absorption trough at 9 keV and could be modeled by a disk wind model (Sim et al. 2008, 2010a; Matzeu et al. 2022) of terminal velocity $v_{\infty} = -0.26 \pm 0.03c$, which implies at least a factor of $\times 2$ increase in wind velocity compared to the original 2017 observation. Thus the wind in PG 1448+273 appears to be strongly variable, both in its opacity and velocity, reminiscent of the drastic velocity changes in MCG-3-58-07 ($v/c \sim 0.07 \rightarrow 0.2$; Braito et al. 2022).

This paper presents a follow-up of the Reeves et al. (2023) work, where subsequently four new simultaneous *XMM-Newton* and *NuSTAR* observations of PG 1448+273 were performed in July and August 2023. The observations were also co-ordinated with daily *Swift* monitoring, to measure the overall variability of PG 1448+273 throughout the campaign. In these new observations, the iron K wind profile is found to be both velocity broadened and blue-shifted up to 10 keV in the X-ray spectra, revealing one of the fastest known ultra fast outflows (UFOs) in an AGN X-ray spectrum. The overall profile can be modeled by a geometrically thick disk wind, which achieves a maximum terminal velocity of $v_{\infty} = -0.43 \pm 0.03c$. The subsequent mass outflow rate is inferred to be close to the Eddington rate in this high accretion rate AGN.

The paper is organized as follows. In Section 2, the observations and data reduction are described, while in Section 3 the AGN variability is quantified through the *XMM-Newton*, *NuSTAR* and *Swift* observations. Section 4 presents the results of the physically motivated disk wind modeling, where the velocity range and mass outflow rate of the AGN wind are inferred. Section 5 quantifies any wind variability

within the 2023 campaign and is compared with past observations. Section 6 then compares the properties of the wind in PG 1448+273 with other AGN, while the wind energetics and plausible launching mechanisms are discussed. Throughout the paper, 90% confidence intervals for one parameter of interest are adopted for the uncertainties (or $\Delta\chi^2 = 2.7$), while parameters are stated in the AGN rest frame at $z = 0.0645$. The standard Λ CDM cosmology ($H_0 = 70 \text{ km s}^{-1} \text{ Mpc}^{-1}$, $\Omega_m = 0.3$, $\Omega_{\Lambda} = 0.7$) is adopted throughout the paper.

2. OBSERVATIONS AND DATA REDUCTION

The 2023 X-ray campaign of PG 1448+273 encompassed four observations with *XMM-Newton* (Jansen et al. 2001) and *NuSTAR* (Harrison et al. 2013) in July–August 2023, with a spacing of about two weeks between each observation; see Table 1 for the observation log of the campaign. The *Swift* campaign consisted of 39 daily X-ray Telescope (XRT, Burrows et al. 2005) snapshots of approximate 1 ks duration from June–August 2023, in order to provide temporal coverage over the entire *XMM-Newton* and *NuSTAR* campaign. The *Swift* XRT data were processed with v0.13.7 of the XRT-PIPELINE to create the lightcurves and spectra. A circular source extraction region of $20''$ was used, while for the background an annulus of radii $40''$ and $130''$ centered on the source was adopted.

The first and third of the *XMM-Newton* observations (hereafter OBS 1 and OBS 3) covered a duration of about a day (86.1 ks and 73.2 ks respectively), as measured from the start and stop times of the sequences (see Table 1). The second *XMM-Newton* observation (OBS 2) was interrupted by a strong Solar flare of 5 hours duration and the telescope filter wheel was subsequently closed during this time (CAL CLOSED position). As a result, the second *XMM-Newton* observation was split into two separate sequences either side of the Solar flare (hereafter OBS 2a and 2b), of duration 11.8 ks and 45.9 ks respectively. The fourth *XMM-Newton* observation (OBS 4) was scheduled as a result of the exposure time lost during the second observation and was of shorter (22.1 ks) duration. Each of the *XMM-Newton* observations were performed simultaneously with *NuSTAR* at hard X-rays. All four *NuSTAR* observations covered a total duration of about 100 ks each, in order to overlap with the start and stop times of each of the *XMM-Newton* exposures, while the fourth *XMM-Newton* observation coincided with the start of the corresponding *NuSTAR* exposure (see Table 1). The *XMM-Newton* EPIC-pn (Strüder et al. 2001) exposures were performed in Large Window mode, with the medium filter applied, while the EPIC-MOS (Turner et al. 2001) exposures were in Small Window mode.

The *XMM-Newton* and *NuSTAR* observations were processed using the NUSTARDAS v2.1.2, *XMM-Newton* SAS v20.0 and HEASOFT v6.30 software. Background screening was performed on the *XMM-Newton* observations, in order to remove periods of high background due to Solar flares during the course of each *XMM-Newton* orbit. A background cut of $> 1 \text{ cts s}^{-1}$ from 10–12 keV over the entire EPIC-pn field of view was applied to select good time intervals of low background for subsequent spectral extraction. While the first and fourth observations were free of background flares, a strong Solar flare affected *XMM-Newton* OBS 2 (as noted above). As a result, the net EPIC-pn exposures were reduced to 6.3 ks and 34.3 ks for the OBS 2a and OBS 2b sequences respectively. A portion of *XMM-Newton* OBS 3 was also affected

TABLE 1
OBSERVATION LOG FOR THE 2023 *XMM-Newton*, *NuSTAR* AND *Swift* CAMPAIGN OF PG 1448+273.

Observation	Sequence	Start Time (UT)	End Time (UT)	Duration (ks)	Net Exp (ks) ^a	Rate(s ⁻¹) ^b	Flux ^c
NuSTAR 1	6092001002	2023/07/05 22:16:09	2023/07/07 03:06:09	103.8	51.7	0.074 ± 0.002	3.2
NuSTAR 2	6092001004	2023/07/17 18:36:09	2023/07/19 00:56:09	109.2	51.1	0.069 ± 0.002	3.0
NuSTAR 3	6092001006	2023/08/02 16:51:09	2023/08/03 23:06:09	108.9	52.4	0.062 ± 0.002	2.7
NuSTAR 4	6092001008	2023/08/17 10:11:09	2023/08/18 15:01:09	103.8	54.2	0.063 ± 0.002	2.8
NuSTAR mean					196.1 ^d	0.069 ± 0.001	3.0
XMM-Newton 1	0920250201	2023/07/06 00:58:34	2023/07/07 00:53:57	86.1	80.3	3.555 ± 0.007	5.9
XMM-Newton 2a	0920250301	2023/07/18 00:09:33	2023/07/18 03:25:52	11.8	6.3	2.108 ± 0.022	3.7
XMM-Newton 2b	0920250301	2023/07/18 08:33:29	2023/07/18 21:18:44	45.9	34.3	3.646 ± 0.010	5.9
XMM-Newton 3	0920250401	2023/08/02 18:11:32	2023/08/03 16:31:34	73.2	53.4	3.216 ± 0.008	5.1
XMM-Newton 4	0920250601	2023/08/17 09:55:40	2023/08/17 16:04:02	22.1	20.6	3.842 ± 0.014	6.1
XMM-Newton mean					188.6 ^d	3.481 ± 0.004	5.8
Swift/XRT (obs 1–39) ^e	00097192	2023/06/25 10:12:35	2023/08/14 11:08:56		35.5 (total)	0.071 ± 0.008 0.389 ± 0.028 0.181 ± 0.013	2.0 (low) 12.3 (high) 5.3 (mean)

^a Net exposure, for *XMM-Newton* (EPIC-pn), *NuSTAR* and *Swift/XRT*, correcting for background screening, SAA passage and detector downtime.

^b Net count rates per *XMM-Newton* (EPIC-pn), *Swift/XRT* or *NuSTAR* observation.

^c Observed flux measured from 0.5–10 keV for *XMM-Newton* (EPIC-pn) and *Swift/XRT* and 3–30 keV band for *NuSTAR*. Units are $\times 10^{-12}$ ergs cm⁻² s⁻¹.

^d The total exposure time of the mean spectrum excludes the short lower flux OBS 2a *XMM-Newton* sequence and the corresponding dip portion of the 2nd *NuSTAR* observation, from 20–50 ks as measured from the start of that observation (see Figure 2).

^e The minimum, maximum and mean count rates and fluxes are given across all 39 *Swift* XRT observations.

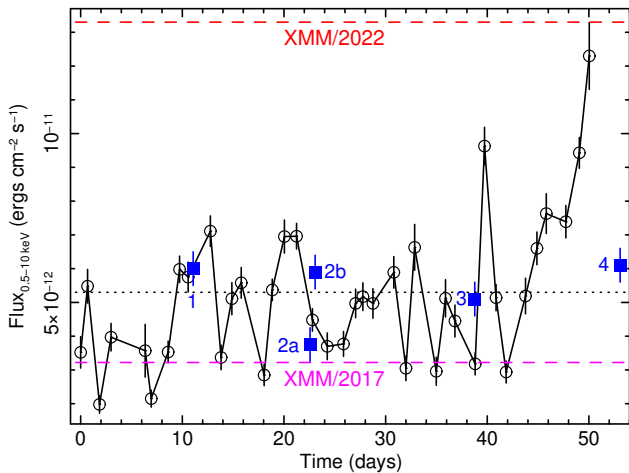


FIG. 1.— *Swift* XRT lightcurve of PG 1448+273 from the 2023 monitoring campaign, where time is measured in days from the start time of the *Swift* monitoring listed in Table 1. The 0.5–10 keV XRT lightcurve (black circles) exhibits a factor of $\times 6$ variability over the whole campaign. In comparison, the 0.5–10 keV flux measured from the 4 *XMM-Newton* observations (blue squares) show little variability between each sequence, with the exception of the short OBS 2a sequence. Overall the *XMM-Newton* observations captured the source close to the average *Swift* flux in the campaign, as is shown by the black dotted horizontal line. In contrast, two previous *XMM-Newton* observations of PG 1448+273 in 2017 and 2022 spanned the range of *Swift* flux, as is indicated by the magenta and red horizontal dashed lines. Thus the 2023 *XMM-Newton* observations resemble an average flux state of PG 1448+273.

by background flares, which resulted in a reduction of the net exposure to 53.4 ks for spectral extraction. The *NuSTAR* exposures were screened for passage through the South Atlantic Anomaly (SAA), resulting in net exposures of between 51–54 ks per FPM module per observation; this is typical of the 50% observing efficiency in a low Earth orbit. Table 1 summarizes all of the resulting exposures.

NuSTAR source spectra were extracted using a 45'' circular region centered on the source and two background circular regions with a 45'' radius and clear from stray light. *XMM-Newton* EPIC-pn spectra were extracted from single and double events (patterns 0–4), using a 35'' source region

and $2 \times 35''$ background regions on the same chip. EPIC-MOS spectra were extracted using patterns 0–12, using a 30'' source region and $2 \times 36''$ background regions. The effective area of the EPIC CCD detectors was corrected at high energies through the SAS task ARFGEN by applying the option APPLYABSFLUXCORR¹². This option provides an improved cross calibration for simultaneous observations between *NuSTAR* and *XMM-Newton* over the overlapping 3–10 keV range. For each observation, the spectra and responses from the individual FPMA and FPMB detectors on-board *NuSTAR* were combined into a single spectrum after they were first checked for consistency. The *NuSTAR* spectra were utilized over the 3–30 keV band; above 30 keV the source spectrum becomes background dominated as the source count rate declines. The total *NuSTAR* background count rate over this band is approximately 6% of the source rate. For EPIC-pn the background rate after filtering is about 4% over the 3–10 keV band and negligible at soft X-rays.

As the effective area of the EPIC-pn detector is about a factor of $\times 8$ larger than that of each EPIC-MOS CCD at 9 keV, where the high energy absorption feature in PG 1448+273 occurs (see Section 4), we used only the EPIC-pn and *NuSTAR* data in the detailed spectral analysis. Nonetheless the MOS spectra are found to be consistent with the EPIC-pn across the 0.3–10 keV band. All the spectra are binned to a minimum of 100 counts per bin to ensure a minimum signal to noise ratio of 10 in the spectra and χ^2 minimization was used for the subsequent spectral fitting. Count rates and fluxes for each of the exposures are listed in Table 1.

Spectra from the *XMM-Newton* Reflection Grating Spectrometer (RGS, den Herder et al. 2001) for all of the 2023 observations were extracted using the RGSPEC pipeline. These were combined into a single RGS 1+2 spectrum for each observation using using RGS COMBINE, after first checking that the individual RGS 1 and RGS 2 spectra were consistent with each other within the errors. Furthermore, very little variability was observed over the 4 epochs (OBS 1, 2b, 3,

¹² <https://xmmweb.esac.esa.int/docs/documents/CAL-SRN-0388-1-4.pdf>

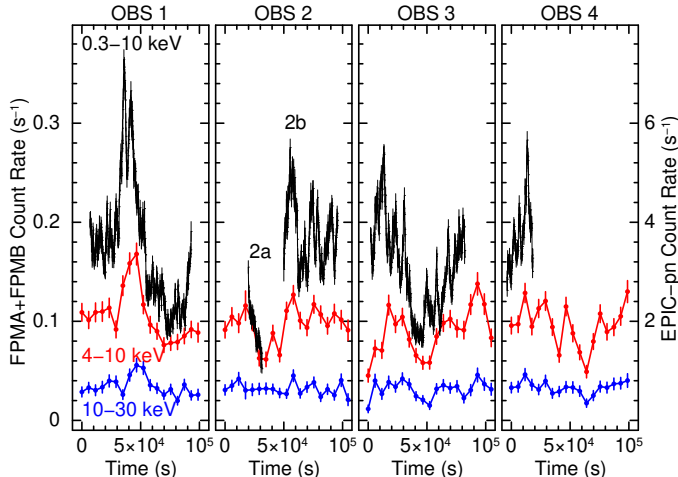


FIG. 2.— Background subtracted lightcurves from the 2023 *XMM-Newton* and *NuSTAR* observations of PG 1448+273. The x-axis shows the time elapsed for each observation, compared to the start time of each *NuSTAR* exposure, while the y-axis shows the count rates for *NuSTAR* (FPMA+FPMB) and EPIC-pn (right-hand axis). The 0.3–10 keV EPIC-pn lightcurve is shown in black in 200 s bins, while *NuSTAR* is shown in red and blue, over the 4–10 keV and 10–30 keV bands respectively and are binned into 5814 s orbital bins. Note the gap in *XMM-Newton* OBS 2, split into 2 sequences (2a and 2b as marked), was due to the Solar flare which interrupted the observation. Overall the average source flux was similar between each of the observations, while a notable flare was observed in OBS 1 and OBS 2a appears to coincide with a short dip in the lightcurve. The variability amplitude in the hardest 10–30 keV band is modest in comparison.

4) in the RGS band; the 0.4–2.0 keV flux ranged between $3.6 - 4.1 \times 10^{-12} \text{ ergs cm}^{-2} \text{ s}^{-1}$, while no spectral variations were seen. As a result, all of these epochs were combined into a single 2023 RGS spectrum to maximize signal to noise, with the exception of the very short OBS 2a sequence, which has very low S/N. The total net count rate obtained over the 6–30 Å band (RGS 1+2 combined) was $0.195 \pm 0.001 \text{ cts s}^{-1}$, with a net exposure of 141.7 ks. The spectra were binned in constant wavelength bins of $\Delta\lambda = 0.1 \text{ Å}$, which approximates the spectral resolution of the RGS gratings.

3. OVERALL AGN VARIABILITY

Figure 1 shows the fluxed *Swift* XRT lightcurve of PG 1448+273 during the 2023 campaign. Here, the AGN displayed a factor of $\times 6$ variability, ranging in 0.5–10 keV flux from $2 - 12 \times 10^{-12} \text{ ergs cm}^{-2} \text{ s}^{-1}$. Several mini X-ray flares are apparent in the lightcurve, the most notable occurring at the end of the *Swift* monitoring. For comparison, the mean flux of each of the *XMM-Newton* observations are overlaid on the Figure 1 lightcurve as blue squares. In contrast to the variability amplitude caught by *Swift*, each of the *XMM-Newton* observations (OBS 1, 2b, 3, 4) caught the source at a very similar flux, covering a narrow range from $F_{0.5-10 \text{ keV}} = 5.1 - 6.1 \times 10^{-12} \text{ ergs cm}^{-2} \text{ s}^{-1}$ and close to the mean *Swift* flux of $F_{0.5-10 \text{ keV}} = 5.3 \times 10^{-12} \text{ ergs cm}^{-2} \text{ s}^{-1}$. The only exception to this occurs at the very start of second *XMM-Newton* observation (OBS 2a sequence), where the AGN was seen at a lower flux of $F_{0.5-10 \text{ keV}} = 3.7 \times 10^{-12} \text{ ergs cm}^{-2} \text{ s}^{-1}$. Even the fourth *XMM-Newton* observation caught the AGN close to the average *Swift* flux, despite it occurring a few days after the strong X-ray flare at the end of the *Swift* lightcurve. The lack of any strong variability comparing each of the 2023 *XMM-Newton* observations also contrasts with two recent *XMM-Newton* observations of PG 1448+273 in 2017 and

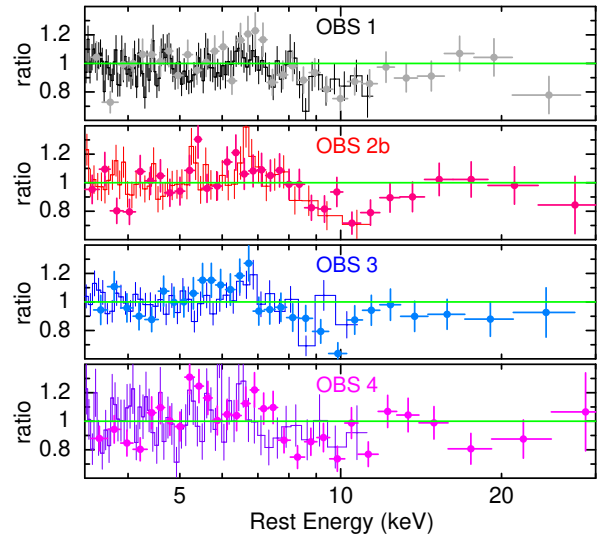


FIG. 3.— The four panels shows the simultaneous *XMM-Newton* and *NuSTAR* (filled circles) spectra for OBS 1, 2b, 3 and 4 (top to bottom), plotted as a ratio to a power-law over the 3–30 keV band. Note the deficit of counts observed from 8–12 keV in each case, highlighting the presence of an absorption trough.

2022, which encompass the range of fluxes observed in the *Swift* lightcurve, see Figure 1. In contrast, the four 2023 *XMM-Newton* observations appear to probe an average flux state of this AGN.

X-ray lightcurves were also extracted for each of the observations over the full 0.3–10 keV band for EPIC-pn, using time bins of 200 s and over the 4–10 keV and 10–30 keV bands for *NuSTAR*, using orbital bins of 5814 s duration; these are plotted in Figure 2. As can be seen from the lightcurves, the mean fluxes across all of the observations are similar, while factor of two variability on shorter kiloseconds timescales is observed. In particular, a strong flare is observed in OBS 1, which is apparent across both the *XMM-Newton* and *NuSTAR* lightcurves, while the start of OBS 2a coincides with a factor of two dip in flux. Unfortunately, the recovery from this dip is missed by *XMM-Newton* as it occurs during the CAL CLOSED segment of OBS 2, although the 4–10 keV band *NuSTAR* lightcurve does capture the dip from 20–50 ks in its entirety. The highest energy band (10–30 keV) exhibits little variability, indicating the intrinsic hard X-ray continuum remained relatively steady over the entire campaign.

4. X-RAY SPECTRAL ANALYSIS

A simple comparison of the individual spectra was then performed across all four of the *XMM-Newton* observations, excluding the very short OBS 2a dip exposure. The *XMM-Newton* spectra were fitted with a simple power-law model modified by Galactic absorption, along with their corresponding simultaneous *NuSTAR* spectra over the 3–30 keV band. Figure 3 shows the spectra plotted as a data-to-model ratio to the above power-law model. None of the spectra show a significant variation in photon index within $\Delta\Gamma = 0.1$ (e.g., OBS 1, $\Gamma = 2.17 \pm 0.03$ vs OBS 4, $\Gamma = 2.23 \pm 0.05$). The hard X-ray flux, as measured by *NuSTAR*, also shows little variation ($F_{3-30 \text{ keV}} = 2.7 - 3.1 \times 10^{-12} \text{ ergs cm}^{-2} \text{ s}^{-1}$). Negative residuals are also present in each of the ratio spectra between 8–12 keV, indicating the presence of iron K absorption and positive residuals are observed between 5–7 keV, indicating emission. Below 3 keV, all of the spectra show a smooth soft X-ray excess above the power-law continuum, with very sim-

ilar fluxes over the four observations (Table 1).

The individual 3–30 keV band spectra were fitted by adding a broadened Gaussian absorption profile to the power-law continuum to model the absorption trough between 8–12 keV. This is well modeled at a rest frame energy of $E = 9.8 \pm 0.4$ keV, with a width of $\sigma = 1.2 \pm 0.5$ keV; this improved the fit statistic from $\chi^2/\nu = 200.4/131$ (power-law only) to $\chi^2/\nu = 147.2/125$ (with absorption profile). The absorption line equivalent width does not vary across the four 2023 epochs, ranging from $EW = -465 \pm 180$ eV (OBS 1) to $EW = -570 \pm 210$ eV (OBS 4); i.e. the values are consistent within the errors. Likewise, allowing the line energy to vary between observations did not improve the fit ($\Delta\chi^2 < 2$), where the energy varies by < 0.5 keV. Thus the iron K absorption profile does not appear to vary between observations.

Thus given the lack of spectral variability across the 2023 observations, a mean spectrum was created for both the EPIC-pn and *NuSTAR* data, in order for the iron K region to be characterized at high signal to noise. The mean spectra include all time intervals, except for the short OBS 2a *XMM-Newton* sequence and the corresponding dip period between 20–50 ks as seen in *NuSTAR* OBS 2 (13.3 ks net exposure). The net exposures of the mean spectra (after background screening), along with their count rates and fluxes are reported in Table 1. The spectra are also plotted in Figure 4 (left panel) which shows the mean fluxed spectra in νF_ν space, after multiplying twice by photon energy and are folded through the instrumental responses. The *XMM-Newton* and *NuSTAR* spectra are in good agreement, allowing for a small cross normalization multiplicative factor between *NuSTAR* and EPIC-pn of $C = 1.14 \pm 0.02$. Note that the background level lies well below the source spectra (by more than an order of magnitude), except for the highest energy *NuSTAR* bin at 30 keV. The spectra clearly reveal the structure in the Fe K region against the steep continuum, with an excess of counts peaking below 6–7 keV and a broad deficit between 8–12 keV, due to an absorption trough. The overall profile resembles the P Cygni like wind profile observed in PDS 456 (Nardini et al. 2015).

A baseline model (model (a)) was constructed to fit the X-ray continuum between 0.3–30 keV. This consisted of two continuum components; a steep ($\Gamma > 2$) power-law to account for the hard X-ray emission and a Comptonized disk component (the COMPTT model within XSPEC, Titarchuk 1994) for the soft X-ray excess. Both of these are modified by the Galactic absorption column of $N_{\text{H}} = 3 \times 10^{20} \text{ cm}^{-2}$ (Kalberla et al. 2005) as modeled by the TBABS model (Wilms et al. 2000). The best fit continuum parameters are reported in Table 2 (model (a)). In addition to the continuum form, a weak soft X-ray emission line is required in the pn spectrum, at an energy of $E = 0.96 \pm 0.02$ keV and an equivalent width of $EW = 5.8 \pm 1.3$ eV. The emission line width is unresolved at the pn resolution, with $\sigma < 0.07$ keV. Its possible origin has been discussed previously in Reeves et al. (2023) from the analysis of the 2022 RGS spectrum and it likely arises from photoionized emission over the Ne band from larger scale gas.

Although the baseline model provides a good description of the soft X-ray band, the overall fit statistic is quite poor, with a reduced chi-squared of $\chi^2/\nu = 764/622$. Strong residuals arise over the 3–30 keV band, in the form of a broad iron K emission and absorption profile (see Figure 4, right panel). Indeed restricting the fit to just the 3–30 keV band yields a reduced chi-squared of $\chi^2/\nu = 315.5/194$, rejected with a

null hypothesis probability of 8×10^{-8} .

To provide an initial non-physical parameterization of the iron K profile, both a Gaussian emission and absorption line were added to the baseline model. This returned a significant improvement in the fit statistic, to $\chi^2/\nu = 643.7/616$, while the fit statistic is also acceptable over the 3–30 keV band ($\chi^2/\nu = 193.7/188$). A broadened emission line was required, at a centroid energy of $E = 6.61 \pm 0.09$ keV, with an equivalent width of $EW = 143 \pm 26$ eV and a line width of $\sigma = 0.30^{+0.16}_{-0.10}$ keV. Interestingly, a very high centroid energy is found for the absorption profile, with $E = 9.8 \pm 0.4$ keV, which is significantly broadened ($\sigma = 1.1^{+0.5}_{-0.4}$ keV) and has a high equivalent width ($EW = -435^{+150}_{-190}$ eV). The parameters are also consistent with those obtained in the individual 2023 sequences. The centroid energy implies a blue-shift of either $v/c \sim -0.33$ or $v/c \sim -0.36$ for an association with either H-like (at 6.97 keV) or He-like iron (at 6.7 keV) respectively. The degree of blue-shift may be amongst the most extreme of those measured in nearby ultra fast outflows to date (Tombsi et al. 2010; Gofford et al. 2013; Igo et al. 2020; Luminari et al. 2021; Matzeu et al. 2023) and is at the highest end of the velocity range inferred for PDS 456 (Matzeu et al. 2017).

For a more physical parameterization of the absorber, the broad Gaussian absorption line was replaced by an XSTAR absorption model (Kallman et al. 2004), using the same absorption grids used in the Reeves et al. (2023) paper on the 2022 datasets. A large turbulence velocity is used, with $v_{\text{turb}} = 25000 \text{ km s}^{-1}$, to parameterize the breadth of the profile. The best fit parameters of the XSTAR model are: $N_{\text{H}} = 6.2^{+1.3}_{-2.1} \times 10^{23} \text{ cm}^{-2}$, $\log \xi = 5.27^{+0.19}_{-0.13}$ and outflow velocity $v/c = -0.34 \pm 0.02$. Note the outflow velocity here corresponds to the point of maximum opacity in the profile, with an effective dispersion on the red and blue wings of $\pm 0.08c$ according to the turbulence velocity. The fit is statistically equivalent to the Gaussian case, with $\chi^2/\nu = 649.9/616$, while the inferred velocity is also consistent. The parameters are in broad agreement with those obtained by Reeves et al. (2023) for the lower flux slice B interval of the 2022 *NuSTAR* observation.

Note in comparison to the broad ionized emission and absorption profile, only an upper-limit can be placed on any narrow 6.4 keV Fe K α fluorescence line, with an equivalent width of < 30 eV. This is consistent with the X-ray Baldwin effect in higher luminosity or higher accretion rate AGN (Iwasawa & Taniguchi 1993; Bianchi et al. 2007)

4.1. Disk Wind Modeling

In order to model the Fe K wind signatures in the PG 1448+273 spectra in a physical context, we utilized the radiative transfer disk wind code developed by Sim et al. (2008, 2010a,b). The disk wind model provides a self consistent treatment of both the emission and absorption arising from a biconical wind, as well as computing the (non-uniform) ionization structure and velocity field through the flow. Photoionization and atomic data are adopted from XSTAR (Kallman et al. 2004). The wind geometry is illustrated in Figure 5; see Matzeu et al. (2022) for a more detailed description.

This model has been previously employed to fit the Fe K wind absorption profiles in several AGN; e.g. Mrk 766 (Sim et al. 2008), PG 1211+143 (Sim et al. 2010a), PDS 456 (Reeves et al. 2014), IZw 1 (Reeves & Braito 2019),

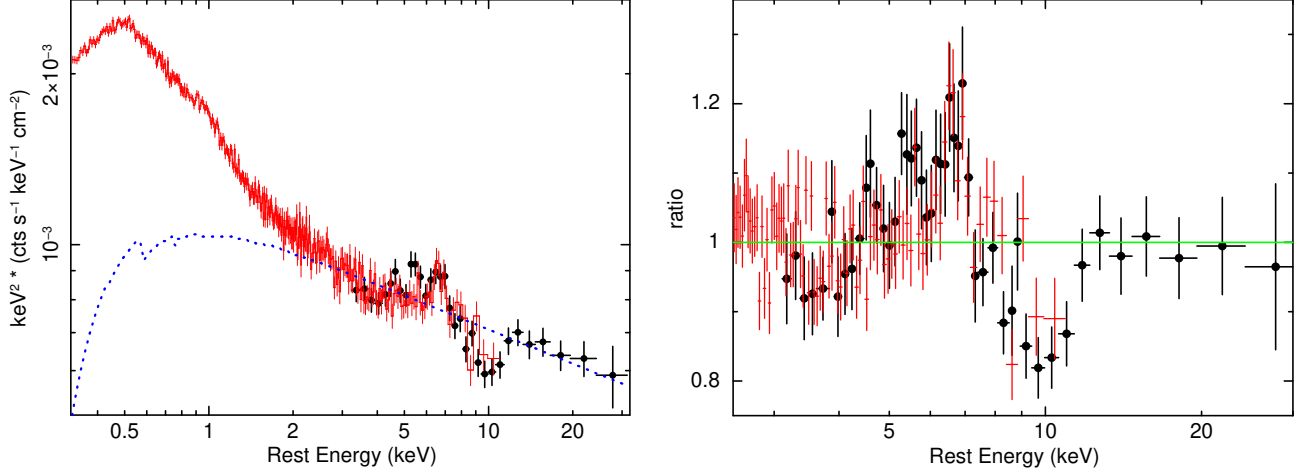


FIG. 4.— Mean *XMM-Newton* EPIC-pn and *NuSTAR* X-ray spectra of PG 1448+273. The pn is shown in red and *NuSTAR* FPMA+B as black circles. The left panel shows the fluxed spectrum, where the count rate spectrum has been divided by the instrumental effective area and multiplied twice by energy and thus the flux is in νF_ν units. The dotted blue line shows the approximate level of the hard X-ray power-law continuum, modified by Galactic absorption. The strong soft X-ray excess is apparent above the power-law. Note the cross normalization factor of $\times 1.14$ between *NuSTAR* and *XMM-Newton* is accounted for in the plot. The right panel shows the data/model ratio to the baseline two component continuum model described in Section 4. Both plots highlight the strong absorption trough centered near 10 keV in the AGN rest frame, while Fe K band emission is observed between 5–7 keV.

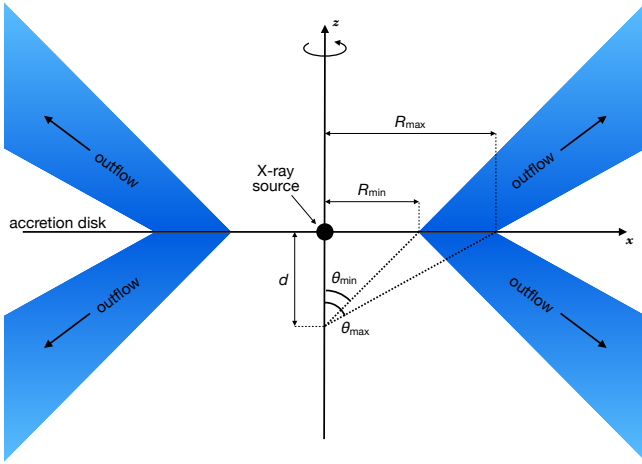


FIG. 5.— Schematic of the disk wind geometry, adapted from Matzeu et al. (2022). The polar (z) and accretion disk axis (x) are shown as solid lines. The inner launching radius on the disk is R_{\min} and the outer launching radius is R_{\max} . In the diskwind models adopted here, the minimum launch radius is set to $32R_g$ (in units of the gravitational radius). The outer launching radius is $R_{\max} = 48R_g$ for the DW thin grid, while for the DW thick case $R_{\max} = 96R_g$. Thus the latter scenario corresponds to a geometrically thicker wind. The minimum opening angle of the wind streamline is θ_{\min} and is given by $\arctan(R_{\min}/d)$. In the models explored here, $R_{\min}/d = 1$ and thus $\theta_{\min} = 45^\circ$. See Matzeu et al. (2022) and Sim et al. (2008, 2010a) for a more detailed model description.

MCG –03–58–007 (Braitto et al. 2022), PG 1126–041 (Giustini et al. 2023) and most recently to the previous X-ray spectra of PG 1448+273 (Reeves et al. 2023). Matzeu et al. (2022) expanded the parameter ranges covered by this wind model and tested the resulting grids on the prototype example of a fast disk wind in PDS 456. The FAST32 grid calculated by Matzeu et al. (2022) for this purpose was also recently applied to the previous (2017, 2022) X-ray spectra of PG 1448+273 (Reeves et al. 2023). Here, we test two variants of the FAST32 disk wind model:-

- A *geometrically thin* accretion disk wind (hereafter DW thin), which is identical to the FAST32 grid calculated by Matzeu et al. (2022). Here the inner launch radius is

$R_{\min} = 32R_g$ (in gravitational units), while the outer launch radius on the disk surface is $R_{\max} = 48R_g$.

- A *geometrically thick* accretion disk wind (hereafter DW thick), where the inner launch radius is $R_{\min} = 32R_g$ and the outer launch radius is increased to $R_{\max} = 96R_g$.

For clarity, we give the velocities and terminal velocities attained in the wind, as originally defined in Sim et al. (2008, 2010a). Consider the velocity as a function of distance along the flow launched at a single point off the disk. This is expressed in a simple analytical form, where the velocity along the flow (v_l) increases versus the length along the flow (l). This is parameterized in Sim et al. (2008), as per their equation 1, where:-

$$v_l = v_0 + (v_\infty - v_0) \left(1 - \frac{R_v}{R_v + l} \right)^\beta. \quad (1)$$

Here v_0 is the initial velocity at launch, while R_v is the radius at which the acceleration starts to occur. In the models adopted here, computed in Matzeu et al. (2022) (see their Table 1), $R_v = R_{\min}$, i.e. the wind accelerates from the launch point, $v_0 = 0$ (the initial outwards velocity is deemed negligible) and $\beta = 1$ (the velocity power-law index). Thus, with the increasing length (l) along the flow, the velocity quickly tends to the terminal velocity, v_∞ .

Furthermore, the wind will not just be launched at a single specific radius, but over multiple radii on the disk, producing a range of terminal velocities originating at different launch radii (between R_{\min} and R_{\max}). The terminal velocities realized in the wind models are determined via the launch radius and the terminal velocity parameter (f_v), where:-

$$v_\infty/c = f_v \sqrt{2/R}, \quad (2)$$

and R is the launch radius in gravitational units. In the spectral fitting, the terminal velocity is adjusted by varying the f_v parameter, where f_v physically corresponds to the scaling factor between the escape velocity at a radius R on the disk and the final terminal velocity. The effect of gravity upon the

terminal velocity is also accounted for in the diskwind model, by extrapolation back to the launch point of a wind streamline. Thus for $f_v = 1$, the wind is launched reaching exactly the escape velocity from the system.

The range in terminal velocities produced by the wind is thus governed by the range in launch radii as well as the f_v parameter. For example, in the case of $f_v = 1.5$, then from equation 2, the terminal velocities attained in the DW thick grid range from $v_\infty/c = 0.21 - 0.375$, where the fastest velocity is launched at the innermost launch radius of $R_{\min} = 32R_g$ and the slowest (outermost radius) at $R_{\max} = 96R_g$. In contrast the DW thin grid covers a much smaller range of terminal velocities over the narrower range of launch radii from $R_{\min} = 32R_g$ to $R_{\max} = 48R_g$; e.g. for $f_v = 1.5$, then $v_\infty/c = 0.31 - 0.375$. Thus the thicker the streamline is in terms of R_{\max}/R_{\min} , the greater the range of velocities realized by the wind. As a result, the DW thick grid will tend to produce broader absorption profiles due to a larger velocity shear, as the sightline through the wind can intercept a wider range of terminal velocities compared to the DW thin case. The free parameters in the model are then:-

- The terminal velocity parameter, f_v , which covers the range from $f_v = 0.25 - 2.0$ and determines the range of terminal velocities computed.
- The inclination angle $\mu = \cos \theta$, where θ is measured with respect to the polar axis and the minimum wind opening angle (θ_{\min}) is set at 45° (see Figure 5).
- The mass outflow rate normalized to the Eddington rate, where $\dot{M} = \dot{M}_{\text{out}}/\dot{M}_{\text{Edd}}$.
- The ionizing X-ray luminosity (L_X), which is the percentage of the 2–10 keV luminosity to the Eddington luminosity (i.e. $\% L_{2-10\text{keV}}/L_{\text{Edd}}$).
- The photon index of the input X-ray continuum, which is set to that of the hard X-ray power-law (e.g. $\Gamma = 2.2$ for PG 1448+273). As noted in Matzeu et al. (2022), a steeper Γ gives stronger absorption lines, due to the weaker ionizing hard X-ray continuum.

Note as both the mass outflow rate and ionizing luminosity are in Eddington units and the wind radius is in gravitational units, the parameters are invariant to the black hole mass.

The above disk wind grids were applied to the mean 2023 spectrum over the 0.3–30 keV band. The same two component baseline continuum was applied (model (a)), where the residuals over the iron K band reveals the wind profile of PG 1448+273 in emission and absorption (Figure 6, panel (a), $\chi^2/\nu = 764.0/622$). Initially a single fast DW thin zone is added to the baseline model (model (b), see Table 2 for parameters). However, while this is able to account for the spectral residuals between 10–12 keV, at the blue-wards end of the profile, it does not account for the absorption profile between 8–10 keV, while some of emission remains un-modeled between 6–7 keV (see Figure 6, panel (b), $\chi^2/\nu = 685.8/618$). Essentially, the absorption profile predicted by thin wind is not broad enough to account for the whole profile, as the range of terminal velocities achieved is insufficient. A second DW thin zone was then added to the model (model (c), Table 2) and at a lower terminal velocity in order to account for the remaining residuals. This improves the fit statistic further (Figure 6, panel (c), $\chi^2/\nu = 660.8/616$), modeling most

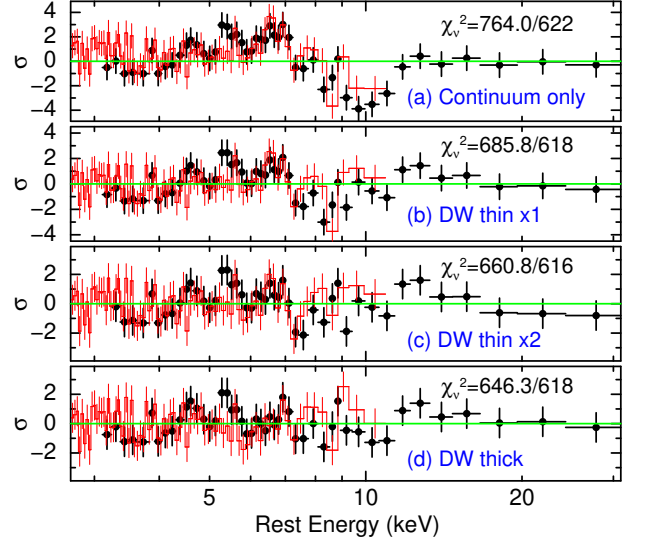


FIG. 6.— Residuals, in units of (data–model)/error, to the mean 2023 spectrum, plotted over the iron K band. Panel (a) shows the residuals to the baseline continuum (no wind), panel (b) shows the case of a single DW thin grid, panel (c) corresponds to two DW thin zones and panel (d) corresponds to the best-fit scenario of a single DW thick zone. In each case, the parameters are reported in Table 2. A geometrically thick disk wind (model (d)) best accounts for the Fe K profile in PG 1448+273.

of the lower energy residuals, although some remain over the 7–10 keV band. Essentially this solution requires two distinct wind zones, where the fastest zone has a maximum terminal velocity of $v_\infty/c = -0.39 \pm 0.03$, modeling the blue-wards extent of the profile, and a slower zone where the maximum velocity attained is $v_\infty/c = -0.23 \pm 0.03$. The parameters of the two velocity wind are reported in Table 2 (models (b) and (c) for the two zones). Note the parameters of the faster zone do not change significantly (within errors) upon the addition of the second slower zone.

The two zone solution requires two distinct velocity components, yet in this scenario both are assumed to be launched over the same radial range on the disk ($32 - 48R_g$). A more physical representation may correspond to the case of a geometrically thick wind, where the dispersion in terminal velocity is naturally produced over a wide range of disk radii, as $v_\infty \propto R^{-1/2}$ and $R = 32 - 96R_g$ in this case. The DW thick grid provides a good account of the whole iron K band profile (Figure 6, panel (d)) and is also statistically the best-fit solution ($\chi^2/\nu = 646.3/618$). The best-fit wind parameters for the DW thick grid are reported in Table 2 (model (d)). Note the inclination angle of $\mu = 0.58 \pm 0.03$ (or $\theta \sim 55 \pm 2^\circ$), is consistent with the previous modeling of the 2017 and 2022 observations (Reeves et al. 2023) and is well within the wind opening angle at 45° . In this model, a wide range of terminal velocities are realized; at the inner streamline the maximum terminal velocity is $v_{\max,\infty} = -0.43 \pm 0.03c$, while for the outer streamline the minimum terminal velocity is $v_{\min,\infty} = -0.25 \pm 0.02c$. The mean terminal velocity, averaged over all launch radii, is $\langle v_\infty/c \rangle = -0.34 \pm 0.03$. This is in agreement with the outflow velocity obtained from the simple XSTAR absorber.

As a result of the wider velocity dispersion within the thick wind, it is able to model the breadth of the absorption profile, unlike the case of a single DW thin zone. This is illustrated in Figure 7, where panel (a) shows the spectrum fitted with the DW thick model and panel (b) shows the resulting Fe K profile from the wind. For the latter plot, the DW thick

TABLE 2
RESULTS OF SPECTRAL FITTING TO MEAN 2023 SPECTRUM.

Parameter	Value
(a) Baseline Continuum:-	
Photon Index, Γ	2.20 ± 0.03
Power-Law Normalization (N_{PL}^a)	1.11 ± 0.04
Cross Normalization ($NuSTAR/EPIC$ -pn)	1.14 ± 0.02
Seed Photon Temperature, T_0 (keV)	0.074 ± 0.004
Comptonization Temperature, kT (keV)	$0.40^{+0.17}_{-0.09}$
Optical Depth (τ)	$8.3^{+1.9}_{-2.0}$
Soft X-ray flux ($F_{0.3-2 \text{ keV}}^b$)	5.4 ± 0.1
Fit Statistic (Baseline only), χ^2/ν	764.0/622
(b) Single Thin Disk Wind (Zone 1):-	
Mass Outflow Rate ($\dot{M}_{out}/\dot{M}_{Edd}$)	0.67 ± 0.10
Ionizing Luminosity (% $L_{2-10 \text{ keV}}/L_{Edd}$)	$1.4^{+0.3}_{-0.2}$
Terminal Velocity Parameter (f_v)	$1.56^{+0.06}_{-0.17}$
Maximum Terminal Velocity ($v_{max,\infty}/c$)	-0.39 ± 0.03
Inclination ($\mu = \cos \theta$)	0.64 ± 0.02
Fit Statistic (Single Thin Wind), χ^2/ν	685.8/618
(c) Additional Thin Disk Wind (Zones 2):-	
Mass Outflow Rate ($\dot{M}_{out}/\dot{M}_{Edd}$)	0.48 ± 0.09
Ionizing Luminosity (% $L_{2-10 \text{ keV}}/L_{Edd}$)	1.4^t
Terminal Velocity Parameter (f_v)	$0.93^{+0.16}_{-0.06}$
Maximum Terminal Velocity ($v_{max,\infty}/c$)	-0.23 ± 0.03
Inclination ($\mu = \cos \theta$)	0.64^t
Fit Statistic (Second Thin Wind), χ^2/ν	660.8/616
(d) Single Thick Disk Wind:-	
Mass Outflow Rate ($\dot{M}_{out}/\dot{M}_{Edd}$)	$0.84^{+0.11}_{-0.12}$
Ionizing Luminosity (% $L_{2-10 \text{ keV}}/L_{Edd}$)	0.80 ± 0.08
Terminal Velocity Parameter (f_v)	1.72 ± 0.12
Maximum Terminal Velocity ($v_{max,\infty}/c$)	-0.43 ± 0.03
Minimum Terminal Velocity ($v_{min,\infty}/c$)	-0.25 ± 0.02
Inclination ($\mu = \cos \theta$)	0.58 ± 0.03
2-10 keV Luminosity, ($L_{2-10 \text{ keV}}^c$)	2.6 ± 0.2
Fit Statistic (Single Thick Wind), χ^2/ν	646.3/618

^a Power-law normalization, in units of $\times 10^{-3}$ photons $\text{cm}^{-2} \text{s}^{-1} \text{keV}^{-1}$ at 1 keV.

^b Observed 0.3–2 keV flux, in units of $\times 10^{-12}$ erg $\text{cm}^{-2} \text{s}^{-1}$.

^c Intrinsic 2–10 keV luminosity, corrected for wind absorption, in units of $\times 10^{43}$ erg s^{-1} .

^t Denotes parameter is tied within the model

model (model d) is compared to the single DW thin model (model b). It is apparent that the DW thick solution predicts a substantially broader profile compared to the DW thin case, where the absorption trough is notably narrower. In addition, the DW thick model also provides a better description of the Fe K emission from the wind.

Interestingly, the mass outflow rate (normalized to Eddington) for the DW thick model is $\dot{M} = 0.84^{+0.10}_{-0.12}$, which is close to Eddington limit. Indeed the confidence contours of \dot{M} versus $v_{max,\infty}$ are well constrained (see Figure 7, panel (c)) in this scenario. The mass outflow rate is also much higher than what was determined from the 2022 *NuSTAR* observation of PG 1448+273. In particular, during the last 60 ks of that observation (slice B), a broad absorption trough was observed centered near 9 keV and the mass outflow rate was inferred to be $\dot{M} = 0.23 \pm 0.06$ (Reeves et al. 2023). The likely reason for this lower value is the adopted wind geometry, where only the thin disk wind model was considered by Reeves et al. (2023) to model the 2022 profile. Instead, the geometrically thicker wind inferred from the higher quality 2023 data naturally requires more mass to achieve a similar line of sight opacity. A comparison of the 2023 versus the 2022 epochs with the DW thick model will be considered in Section 5.

The ionizing X-ray luminosity incident upon the thick wind

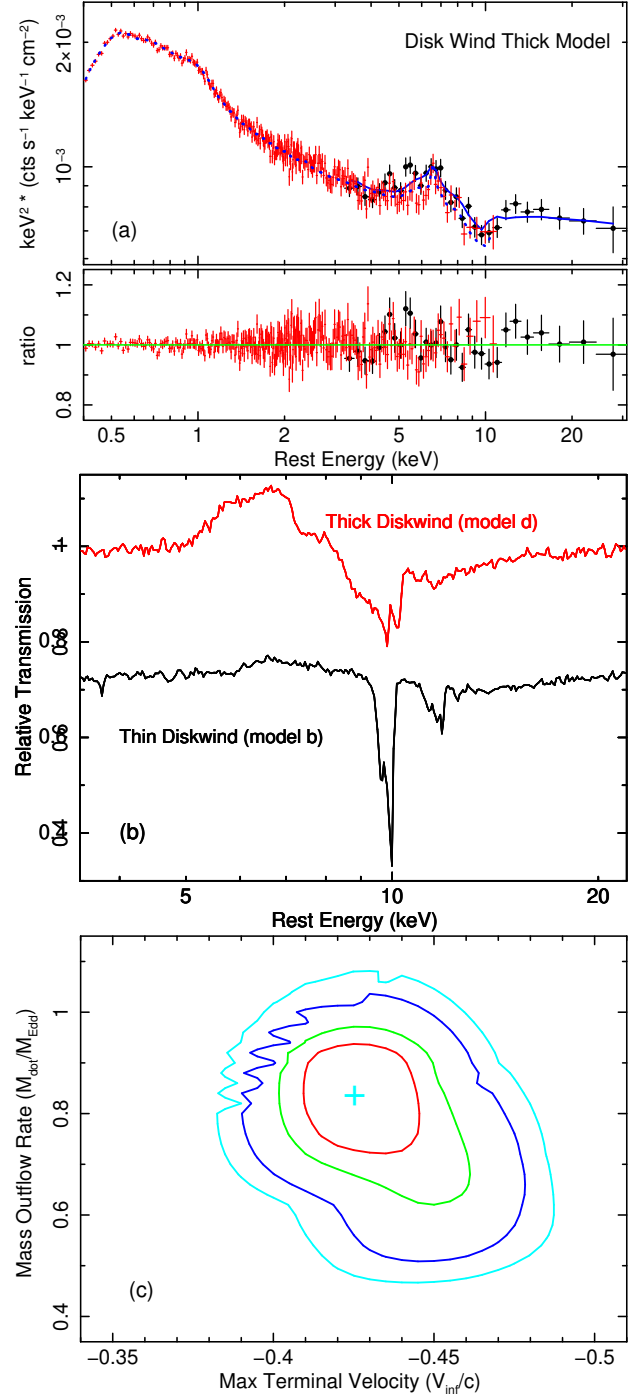


FIG. 7.— Results of the disk wind modeling. Panel (a) shows the best-fit DW thick model fitted to the mean 2023 spectrum. Here, the model (folded through the instrumental responses) is shown as a solid blue line fitted to the *NuSTAR* data from 3–30 keV and as a dotted blue line to the *XMM-Newton* spectrum from 0.3–10 keV. Note the lack of strong soft X-ray absorption. Panel (b) shows the theoretical Fe K profiles predicted from the wind for the DW thick case (red; Table 2, model d) versus the DW thin case (black; Table 2, model b). A y-axis offset has been applied for clarity. The DW thick model produces a broader absorption line profile due to its larger velocity shear, as well as stronger Fe K emission. Panel (c) shows the confidence contours of the mass outflow rate in Eddington units versus the maximum terminal velocity attained by the wind for model (d). The contours represent the 68, 90, 99 and 99.9% confidence levels for two interesting parameters. The mass outflow rate in PG 1448+273 appears to be at nearly the Eddington rate, with a maximum terminal velocity of $v_{max,\infty}/c = -0.43 \pm 0.03$. Note the saw-tooth behavior of the outer contours is due to the finite grid resolution.

is found to be $L_X = 0.80 \pm 0.08\%$, equivalent to the 2–10 keV luminosity being 0.8% of Eddington. This level of X-ray luminosity is high enough such that the most dominant ionic species is H-like iron and little absorption is predicted at soft X-ray energies. This can also be seen from the best-fit spectrum in Figure 7 (panel (a)), where the wind model is featureless at soft X-ray energies and no significant residuals are present. As a consistency check, the above inferred ionizing luminosity can also be compared with the energetics of the AGN. The observed (absorption corrected) 2–10 keV luminosity is $L_{2-10\text{ keV}} = 2.6 \pm 0.2 \times 10^{43} \text{ erg s}^{-1}$ (see Table 2). From the reverberation black hole mass of $M_{\text{BH}} = 1.01^{+0.38}_{-0.23} \times 10^7 M_{\odot}$ (Hu et al. 2021), the Eddington luminosity is $L_{\text{Edd}} = 1.3^{+0.5}_{-0.3} \times 10^{45} \text{ erg s}^{-1}$. Based upon these observables, the expected ratio of the 2–10 keV to Eddington luminosity is $2.0 \pm 0.6\%$. Within the uncertainties, this is comparable (within a factor of two) to the values inferred from the disk wind modeling; here $L_X = 0.80 \pm 0.8\%$ for the DW thick case and $L_X = 1.4^{+0.3}_{-0.2}\%$ for the DW thin case. This suggests the disk wind is just slightly under-ionized when compared to the observed 2–10 keV luminosity.

4.2. Modeling with the Relativistic WINE model

Here we apply the WINE model of Luminari et al. (2018) to provide an alternative parameterization of the wind. The WINE model was originally developed to model the emission profiles resulting from disk winds, motivated by the P-Cygni profile observed in PDS 456 (Nardini et al. 2015). The model has since been extended to self-consistently calculate the wind absorption and has been applied to the wind in the 2017 *XMM-Newton* observation of PG 1448+273 (Laurenti et al. 2021) and to the variable wind of NGC 2992 (Luminari et al. 2023). A forthcoming detailed description of the updated model can be found in Luminari et al. (2024).

In summary, the wind geometry is a conical outflow (see Figure 1, Luminari et al. 2018, 2024), with a half-opening angle of θ_{out} with respect to the polar axis. It is launched at an inner radius of R_0 (in Schwarzschild units of $R_s = 2GM/c^2$), with an initial (innermost) ionization parameter of ξ_0 . The wind absorption is then integrated over a succession of thin shells versus radius as calculated by XSTAR, while the wind emission is integrated over all solid angles and radii. Special relativistic effects are accounted for as described in Luminari et al. (2020, 2021), including the relativistic de-boosting of the continuum as seen by gas expanding radially outwards. The latter effect is important in PG 1448+273 given the large velocities inferred from the iron K absorption profile. In order to calculate the resultant line profiles, a wind density profile of $n(r) = n_0(R/R_0)^{-1}$ is adopted along with a radial velocity profile of $v(r) = v_0(R/R_0)^{-\frac{1}{2}}$; here n_0 and v_0 are the inner number density and velocity at the initial launch radius R_0 . Note the choice of radial profiles is consistent with a momentum conserving wind (e.g. Faucher-Giguère & Quataert 2012), while the velocity profile describes a ballistic trajectory de-accelerating under gravity.

To fit the PG 1448+273 spectrum, the absorption and emission spectra from the WINE model were calculated in the form of two XSPEC multiplicative tables, which modify the same baseline continuum as described earlier. The output parameters for spectral fitting are the inner ionization ($\log \xi_0$), inner velocity (v_0), inner radius (R_0), column density (N_{H}) and half opening angle (θ_{out}). The first three parameters are assumed to be equal in both absorption and emission, except for the

TABLE 3
RESULTS OF FITTING THE WINE MODEL TO THE 2023 SPECTRUM.

Parameter	Value
Fitted Parameters:-	
Absorption column, $N_{\text{H,abs}}/10^{24} \text{ cm}^{-2}$	0.57 ± 0.06
Ionization, $\log(\xi_0/\text{ergs cm s}^{-1})$	5.58 ± 0.04
Inner velocity, v_0/c	0.50 ± 0.02
Inner radius, R_0/R_s	$16.3^{+2.6}_{-1.8}$
Emission column, $N_{\text{H,emiss}}/10^{24} \text{ cm}^{-2}$	1.7 ± 0.3
Half opening angle, θ_{out}	$> 72^\circ$
Photon Index, Γ	2.14 ± 0.02
Fit statistic, χ^2/ν	656.3/618
Derived Parameters:-	
De-boosted luminosity, $L'_{\text{ion}}/10^{43} \text{ ergs s}^{-1}$	2.0 ± 0.2
Inner density, $n_0/10^{10} \text{ cm}^{-3}$	$2.1^{+0.9}_{-0.7}$
Covering fraction, f_{cov}	> 0.69
Mass outflow rate, $\dot{M}_{\text{out}}/M_{\odot} \text{ yr}^{-1}$	$0.14^{+0.05 a}_{-0.04}$
Normalized outflow rate, $\dot{M}_{\text{out}}/\dot{M}_{\text{Edd}}$	$0.61^{+0.23 a}_{-0.17}$

^a The minimum mass outflow rate, corresponding to $f_{\text{cov}} = 0.69$.

column density which may differ along the line of sight versus (on average) across the whole wind. The opening angle is only relevant to the wind emission, as it is calculated over all angles. Note that the inclination between the line of sight and the wind symmetry axis is fixed to 0 degrees, since it cannot be constrained by the data, unlike the diskwind model which adopts a bi-conical geometry with a minimum opening angle of 45° (Figure 5). In WINE, this angle corresponds to a disc observed face-on through a conical, polar wind.

The WINE model produces a good fit to the PG 1448+273 spectrum and in particular over the Fe K band (see Figure 8), with a similar overall fit statistic as per the DW thick case in Section 4.1, with $\chi^2/\nu = 656.3/618$. The fit parameters of the WINE model are listed in Table 3, where the maximum wind launch velocity is $v_0/c = -0.50 \pm 0.02$, just slightly higher than the equivalent maximum terminal velocity obtained by the DW thick model. Note that in the best-fit solution, the minimum wind velocity is $v_{\text{min}} = -0.21c$, while the mass averaged velocity is $v_{\text{avg}} = -0.325c$. This range of velocity is consistent with what was derived from the DW thick grid (model (d), Table 2).

The launch radius is a variable parameter in the WINE model and the best-fit value is $R_0 = 16.3^{+2.6}_{-1.8} R_s$. This is consistent with the inner launch radius (of $32R_g$ or $16R_s$) assumed in the disk wind models in Section 4.1 and demonstrates that such fast winds are likely to be launched from the innermost regions of the accretion disk. The absorption column density is $N_{\text{H,abs}} = 0.57 \pm 0.06 \times 10^{24} \text{ cm}^{-2}$, while the emitter column is higher with $N_{\text{H,emiss}} = 1.7 \pm 0.3 \times 10^{24} \text{ cm}^{-2}$. This may occur if the wind is non-uniform, for instance if the column density is higher at larger θ towards the equatorial direction; this is the case for the diskwind models (higher N_{H} at larger θ). Finally, from the wind emission, the opening angle is constrained to be $\theta_{\text{out}} > 72^\circ$, which corresponds to a lower limit on the wind geometric covering fraction of $f_{\text{cov}} = 1 - \cos(\theta_{\text{out}}) > 0.69$. Indeed the larger the opening angle is, the stronger the wind emission will be.

The innermost density at the launching point of wind is given by the definition of the ionization parameter, where $\xi_0 = L'_{\text{ion}}/n_0 R_0^2$; here L'_{ion} is the 1–1000 Rydberg ionizing luminosity corrected for the de-boosting of the continuum radiation. Following Luminari et al. (2020, 2023), the

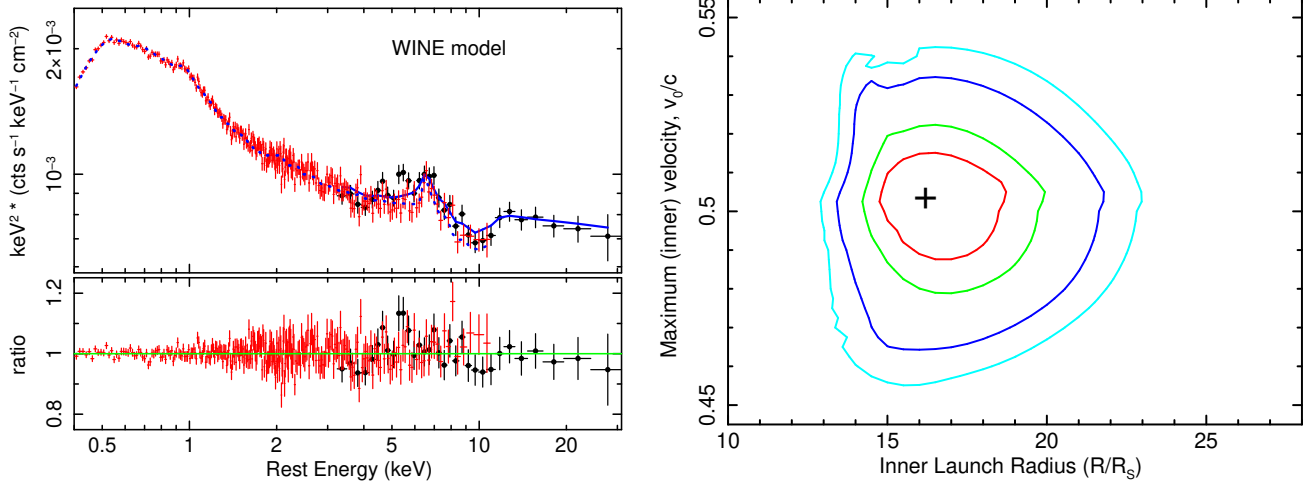


FIG. 8.— Results of modeling the mean 2023 PG 1448+273 spectrum with the relativistic WINE wind model (Luminari et al. 2018). The left panel shows the best fit fluxed spectrum, where the folded counts spectrum has been multiplied twice by energy. The WINE model is shown as a blue line (solid for *NuSTAR*, dotted for EPIC-pn) and reproduces well the iron K absorption and emission profile, as is seen by the data/model residuals. The right panel shows the 68%, 90%, 99% and 99.9% confidence intervals of the maximum wind velocity (v_0/c , at the innermost radius) versus the inner launch radius (R_0), where the latter is in units of the Schwarzschild radius (R_s). In the best-fit scenario, the wind is launched from a radius of $R_0 = 16R_s$ at a maximum velocity of $0.5c$.

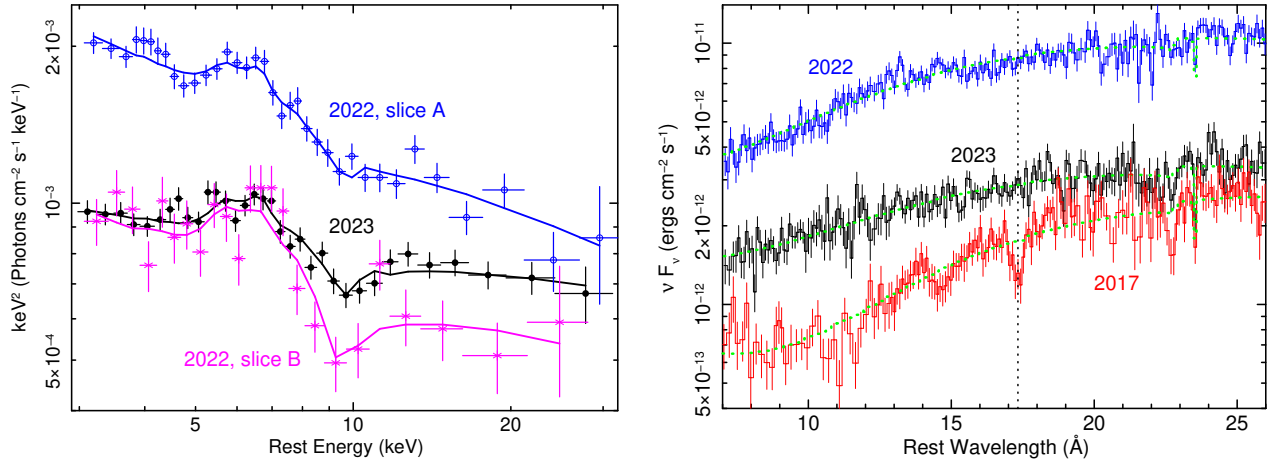


FIG. 9.— Comparison of the PG 1448+273 spectra over different epochs from 2017–23. The left panel shows the the mean 2023 versus the 2022 A (slice A) and 2022 B (slice B) *NuSTAR* spectra, fitted with the thick diskwind model in each case. The spectral differences between each epoch can be accounted for via changes in ionization through the variations in X-ray luminosity, as well as in photon index. Note there was no *NuSTAR* observation in 2017. The right panel shows the comparison of the 2017, 2022 and 2023 RGS spectra. Significant soft X-ray wind absorption was only detected in the low flux 2017 spectrum, in the form of a blueshifted O VIII Ly- α line, as marked by the dotted vertical line.

de-boosted luminosity is given by $L'_{\text{ion}} = \left(\frac{1-v}{1+v}\right)^{\frac{2+\Gamma}{2}} L_{\text{ion}}$, where Γ is the photon index and this also accounts for the redshift of the continuum as seen by the wind. Extrapolation of the best-fit baseline continuum model from 1–1000 Rydberg gives $L_{\text{ion}} = 2.0 \pm 0.2 \times 10^{44} \text{ erg s}^{-1}$, while from the above the continuum is de-boosted by a factor of $\times 10$ for $v_0/c = 0.5$ and $\Gamma \approx 2.2$. Thus the resultant de-boosted luminosity is $L'_{\text{ion}} = 2.0 \pm 0.2 \times 10^{43} \text{ erg s}^{-1}$ and the innermost density is $n_0 = 2.1^{+0.9}_{-0.7} \times 10^{10} \text{ cm}^{-3}$.

From this and the best fit parameters in Table 3, the mass outflow rate is calculated as per Laurenti et al. (2021):-

$$\dot{M}_{\text{out}} = 2 \mu m_p \int_0^{2\pi} \int_0^{\theta_{\text{out}}} \int_{r_0}^{r_1} n(r) v(r) r \sin \theta dr d\theta d\phi, \quad (3)$$

where μ , m_p are the mean atomic mass per proton and the proton mass, respectively. The wind outer radius, r_1 , is calculated analytically from the integral of the density to calculate the absorption column density, while the factor of $\times 2$

arises from summing both hemispheres of the wind. From this integral and the radial velocity and density profiles as above, the mass outflow rate is determined to be $\dot{M}_{\text{out}} = 0.21^{+0.08}_{-0.06} f_{\text{cov}} M_{\odot} \text{ yr}^{-1}$. The lower limit of $\theta_{\text{out}} > 72^\circ$ then yields $f_{\text{cov}} > 0.69$. Thus the minimum mass outflow rate is $\dot{M}_{\text{out}} = 0.14^{+0.05}_{-0.04} M_{\odot} \text{ yr}^{-1}$. For an accretion disk efficiency of $\eta = 0.1$ and the black hole mass of PG 1448+273 (Hu et al. 2021), this corresponds to a normalized rate of $\dot{M}_{\text{out}}/\dot{M}_{\text{Edd}} = 0.61^{+0.23}_{-0.17}$ (or $\dot{M}_{\text{out}}/\dot{M}_{\text{Edd}} = 0.91^{+0.35}_{-0.26}$ for $f_{\text{cov}} = 1$). This is consistent with the mass outflow rate inferred by the disk wind model in Section 4.1.

5. WIND VARIABILITY

To test for any wind variability, the DW thick model in Section 4.1 was applied to the four individual 2023 sequences (OBS 1, 2b, 3, 4), including both the *XMM-Newton* and *NuSTAR* spectra over the 0.3–30 keV band. Note the short (dipping) OBS 2a segment was not included, as its net exposure (6 ks with EPIC-pn) is too short to derive any useful wind

TABLE 4
RESULTS OF SPECTRAL FITTING TO OBS 1–4.

Parameter	OBS 1	OBS 2b	OBS 3	OBS 4
Photon Index, Γ	2.18 ± 0.03	2.11 ± 0.04	2.15 ± 0.04	2.22 ± 0.04
Power-Law Normalization (N_{PL}^a)	1.28 ± 0.06	1.24 ± 0.08	1.07 ± 0.07	1.38 ± 0.09
2–10 keV flux ($F_{2-10\text{keV}}^b$)	2.22	2.17	1.82	2.16
Mass Outflow Rate ($\dot{M}_{\text{out}}/\dot{M}_{\text{Edd}}$)	0.73 ± 0.19	$1.20^{+0.15}_{-0.20}$	$1.05^{+0.18}_{-0.20}$	$0.90^{+0.13}_{-0.20}$
Ionizing Luminosity ($\% L_{2-10\text{keV}}/L_{\text{Edd}}$)	0.80 ± 0.13	0.80^t	0.80^t	0.80^t
Maximum Terminal Velocity ($v_{\text{max},\infty}/c$)	-0.46 ± 0.03	-0.48 ± 0.04	-0.44 ± 0.03	-0.43 ± 0.04
Minimum Terminal Velocity ($v_{\text{min},\infty}/c$)	-0.27 ± 0.02	-0.28 ± 0.03	-0.25 ± 0.02	-0.25 ± 0.03
Inclination ($\mu = \cos \theta$)	0.58 ± 0.04	0.58^t	0.58^t	0.58^t
Fit Statistic (χ^2/ν)	776.9/706	523.9/527	588.5/582	453.7/442

^a Power-law normalization ($\times 10^{-3}$ photons $\text{cm}^{-2} \text{s}^{-1} \text{keV}^{-1}$ at 1 keV).

^b Observed 2–10 keV flux, in units of $\times 10^{-12}$ erg $\text{cm}^{-2} \text{s}^{-1}$.

^t Denotes parameter is tied within the model

TABLE 5
COMPARISON BETWEEN THE 2023 AND 2022 *NuSTAR* SPECTRA.

Parameter	2023	2022A	2022B
Γ	2.16 ± 0.03	2.42 ± 0.04	2.31 ± 0.09
N_{PL}^a	1.29 ± 0.08	3.67 ± 0.22	1.53 ± 0.23
$F_{2-10\text{keV}}^b$	2.38 ± 0.15	4.71 ± 0.28	2.25 ± 0.34
$\dot{M}_{\text{out}}/\dot{M}_{\text{Edd}}$	0.91 ± 0.22	$0.79^{+0.21}_{-0.19}$	$0.92^{+0.32}_{-0.31}$
$\% L_{2-10\text{keV}}/L_{\text{Edd}}$	$0.58^{+0.13}_{-0.11}$	1.16^t	0.58^t
$v_{\text{max},\infty}/c$	-0.42 ± 0.02	-0.42^t	0.42^t
$\mu = \cos \theta$	0.61 ± 0.03	0.61^t	0.61^t
χ^2/ν	55.8/62	103.0/104	26.3/21

^a Power-law normalization ($\times 10^{-3}$ photons $\text{cm}^{-2} \text{s}^{-1} \text{keV}^{-1}$).

^b Flux in units of $\times 10^{-12}$ erg $\text{cm}^{-2} \text{s}^{-1}$.

^t Denotes parameter is tied within the model

constraints, although overall its spectrum is harder with $\Gamma = 1.93 \pm 0.07$. The wind parameters in each case are reported in Table 4. The results are very similar to the mean spectrum, with no significant variation in the maximum terminal velocity of the wind; i.e. from $v_{\text{max},\infty}/c = -0.43 \pm 0.04$ (OBS 4) to $v_{\text{max},\infty}/c = -0.48 \pm 0.04$ (OBS 2b). Neither is there any strong variability in the X-ray flux across the epochs. The mass outflow rate also remains steady and close to Eddington across the four epochs, ranging from $\dot{M} = 0.73 \pm 0.19$ (OBS 1) to $\dot{M} = 1.20^{+0.15}_{-0.20}$ (OBS 2b). This implies there is no significant intrinsic wind variability across the 40 day campaign.

We also compare the properties of the wind in the 2023 mean spectrum with those in the 2022 *NuSTAR* observations (Reeves et al. 2023). Here we apply the DW thick model to both epochs for consistency. As described in Reeves et al. (2023), the 2022 *NuSTAR* observation was split into two slices (slice A and slice B) either side of a factor of $\times 2$ drop in flux. The slice A spectrum covered the first 190 ks in duration of the 2022 *NuSTAR* observation, where the source is brightest ($F_{2-10\text{keV}} = 4.7 \times 10^{-12}$ ergs $\text{cm}^{-2} \text{s}^{-1}$) and the spectrum was relatively featureless. Then in the last 60 ks of the observation, the flux dropped by a factor of two, reaching a similar level to what is observed in the mean 2023 observation and where a strong absorption trough emerged between 8–12 keV.

The three *NuSTAR* spectra (2022 A, 2022 B and 2023) were then fitted with the DW thick grid (model (d)), adopting a simple power-law continuum covering the 3–30 keV hard X-ray band. These are shown in Figure 9 (left panel), while the results are reported in Table 5. Given the factor of two dif-

ference in luminosity between the brighter 2022 A spectrum versus the 2022 B and 2023 spectra, the ionizing luminosity (L_X) was set to be a factor of two higher for the former case. Similar to what was found above, the mass outflow rate is consistent between all three epochs and thus any difference in the opacity of the wind at iron K simply arises from the higher luminosity of the 2022 A spectrum, which serves to increase the wind ionization. Thus across the 2022 and 2023 epochs, no intrinsic variations in the wind parameters appear to be observed and they are consistent with a constant terminal velocity and mass outflow rate. The spectral changes can mainly be explained by variations in the X-ray luminosity, along with changes in the photon index.

Finally the soft X-ray wind properties are compared from the respective *XMM-Newton* RGS epochs. The mean 2023 RGS spectrum versus the 2022 and 2017 epochs is shown in Figure 9 (right panel). The 2023 RGS spectrum is virtually featureless, with no strong emission or absorption within the 3σ level, and it can be fitted with the baseline continuum model of Section 4 with an acceptable fit statistic ($\chi^2/\nu = 242.8/218$). This is in contrast with the 2017 low X-ray flux epoch, where significant soft X-ray wind features were observed from O VIII in particular; see Kosec et al. (2020); Reeves et al. (2023). The vertical line on Figure 9 marks the position of the strong and broadened O VIII Ly α absorption line in the 2017 spectrum, occurring at $\lambda = 17.3 \pm 0.1 \text{ \AA}$ (rest frame) and blue-shifted by $\sim 0.1c$ with respect to the expected wavelength of 18.9 \AA . Indeed, in Reeves et al. (2023) a diskwind model with this velocity could account for both the O VIII and Fe K band absorption in the 2017 epoch. In contrast, no such soft X-ray outflow is found in either the 2023 or the bright 2022 epoch, with upper-limits on the equivalent width of O VIII line of $< 1.4 \text{ eV}$ and $< 1.8 \text{ eV}$ for 2023 and 2022 respectively, versus an equivalent width of $5.1 \pm 1.8 \text{ eV}$ in 2017. This result is consistent with the lack of soft X-ray absorption from the 2023 disk wind modeling and suggests the wind is of an overall higher ionization compared to the low flux 2017 epoch.

6. DISCUSSION

NuSTAR and *XMM-Newton* observations of PG 1448+273 in 2023 have revealed a remarkable ultra fast outflow, with one of the most extreme blue-shifts measured to date among UFO sources. The Fe K band absorption can be parameterized by a simple Gaussian line profile, with a centroid energy of $9.8 \pm 0.4 \text{ keV}$, which, if it is associated to Fe XXVI Ly α , implies an average blueshift of $v/c = -0.33 \pm 0.02$ after ac-

counting for the special relativistic correction on the velocity along the line of sight. This is also consistent with the mean velocity obtained from the best fitting thick disk wind model, of $\langle v/c \rangle = -0.34 \pm 0.02$, as is described in Section 4.1 (see Table 2, model d). The velocity width of the Fe K absorption profile is also pronounced, where $\sigma = 1.1^{+0.5}_{-0.4}$ keV, equivalent to $\sigma_v \sim 0.1c$. This implies a considerable velocity shear, as a result of a range of velocities intercepted along our sightline through the wind. This can be accounted for by the geometrically thick disk wind model, launched over a wide range in radii, where the terminal velocity reaches a maximum value of $v_{\max, \infty} = -0.43 \pm 0.03c$ at the inner edge of the wind, with a minimum velocity of $v_{\min, \infty} = -0.25 \pm 0.02c$ at the outermost radius. The velocity dispersion of $\Delta v = \pm 0.1c$ within the wind is consistent with the Gaussian line width as measured above. Similar results were also found for the relativistic WINE model, where the maximum wind velocity was found to be $v_0/c = -0.50 \pm 0.02$. From the wind emission, the half opening angle of the wind was constrained by WINE to be $\theta_{\text{out}} > 72^\circ$ and covering $> 2\pi$ steradian solid angle.

6.1. Comparison with other winds

Thus the wind profile in PG 1448+273 resembles the P-Cygni like profile in PDS 456 (Nardini et al. 2015), with broad structure due to emission and absorption from a wide angle outflow. The outflow velocity in PG 1448+273 appears to be at the higher end of what has been measured in the prototype UFO in PDS 456, which typically spans the range between $v/c = 0.25 - 0.35$ (Matzeu et al. 2017). Note that in some epochs the fastest outflow component in PDS 456 can also reach values exceeding $0.4c$ (Reeves et al. 2018). A similarly high terminal velocity of $v_\infty = -0.38 \pm 0.02c$ has been reported based upon the disk wind modeling of the similarly luminous QSO, IRAS F11119+3257 (Lanzuisi et al. 2024). Such velocities may appear to be more commonplace in the most luminous AGN at the peak of the quasar epoch at high redshifts; see Chartas et al. (2021) and references therein.

The velocity measured in PG 1448+273 is much higher than what has been measured in samples of other nearby (e.g. $z < 0.1$) AGN (Tombesi et al. 2010; Gofford et al. 2013). For illustration, Figure 10 compares the mean disk wind velocity measured in PG 1448+273 with the distributions of velocities obtained from the *XMM-Newton* and *Suzaku* UFO samples of Tombesi et al. (2010) and Gofford et al. (2013) respectively. In the Tombesi et al. (2010) sample, the mean velocity is $v/c \approx -0.1$, while the distribution of Gofford et al. (2013) is skewed to lower velocities, with a median velocity of $v/c = -0.056$. There are no AGN across either sample where the outflow velocity exceeds $-0.3c$. This is also similar to what was found in Igo et al. (2020), where the absorption lines were detected through the excess variance spectra of nearby AGN. Likewise, a similar range of velocity was also obtained in the SUBWAYS sample of Matzeu et al. (2023), which consists of a sample of QSOs at intermediate redshifts ($z = 0.1 - 0.4$).

Furthermore the equivalent width of the iron K absorption line in PG 1448+273, with $\text{EW} = -435^{+150}_{-190}$ eV, is much higher than those in other nearby AGN; for instance in the Gofford et al. (2013) sample the highest equivalent width is 150 eV with a mean of 40 eV (e.g. see their Figure 7), while similar values were also reported by Tombesi et al. (2010). Thus among these local AGN, PG 1448+273 has one of the highest reported outflow velocities, while the equivalent width

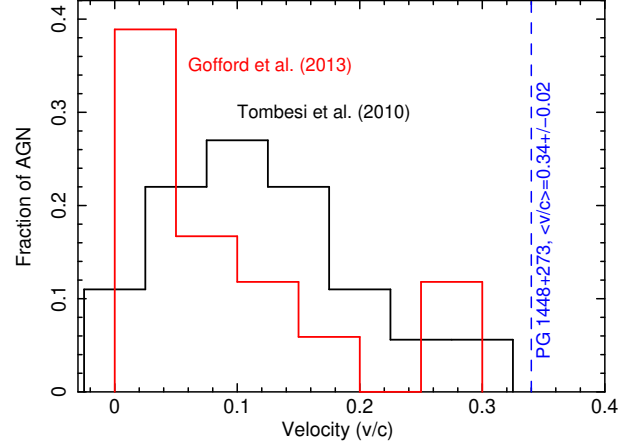


FIG. 10.— The distribution of wind velocities obtained from two samples of nearby ultra-fast outflows (Tombesi et al. 2010; Gofford et al. 2013), versus the wind velocity in PG 1448+273 observed in 2023. The mean velocity in Tombesi et al. (2010) is close to $-0.1c$, while the median velocity of the Gofford et al. (2013) sample is $-0.056c$, both of which are considerably lower than the average terminal velocity of $\langle v/c \rangle = -0.34 \pm 0.02$ attained by the PG 1448+273 wind as measured by the DW thick model. Note an even higher value of $v_\infty/c = -0.43 \pm 0.03$ was found for the maximum terminal velocity. Neither of the Tombesi et al. (2010) and Gofford et al. (2013) samples contain a wind exceeding $> 0.3c$ in comparison.

is substantially higher. This implies a more powerful wind compared to the predominantly broad lined Seyfert 1 galaxies studied by Tombesi et al. (2010) and Gofford et al. (2013). In this regard, PG 1448+273 resembles the UFOs reported in other NLS1s, with velocities at the higher range of the AGN distribution from $0.2 - 0.3c$ and where the absorption features have higher optical depths; e.g. IRAS 13224–3809 (Parker et al. 2017; Pinto et al. 2018; Chartas & Canas 2018), 1H0707–495 (Hagino et al. 2016; Kosec et al. 2018), I Zw 1 (Reeves & Braito 2019), WKK 4438 (Jiang et al. 2018).

It appears plausible that the high accretion rates in NLS1s are more conducive for driving a more powerful wind, as they accrete at high Eddington ratios, have strong UV emission and generally have steep X-ray spectra with weak hard X-ray emission (Giustini & Proga 2019). The latter effect is important, as steep, hard X-ray weak SEDs will tend to produce deeper X-ray wind features due to the gas being less ionized. This was illustrated in the disk wind simulations of Matzeu et al. (2022) (see their Figure 3), where the Fe K absorption profile becomes progressively stronger as the power-law photon index increases from $\Gamma = 1.6$ to $\Gamma = 2.4$, with the equivalent widths increasing to up to hundreds of eV in the steepest sources. It is also consistent with the observed properties of PG 1448+273, which has an intrinsically steep hard X-ray spectrum ($\Gamma = 2.2 - 2.4$) and a relatively low inferred ratio of X-ray to bolometric luminosity; e.g. $L_{2-10\text{keV}}/L_{\text{Edd}} \approx 1\%$.

6.2. The Variable Wind of PG 1448+273

The velocities of UFOs have been shown to vary in several AGN. Some of the most notable cases reported to date occur in: APM 08279+5255 (Saez & Chartas 2011), PDS 456 (Matzeu et al. 2017), IRAS 13224–3809 (Chartas & Canas 2018) and MCG–03–58–007 (Braito et al. 2021, 2022). PG 1448+273 also appears to exhibit substantial variability in its terminal velocity across epochs, which may vary by up to a factor of four. *XMM-Newton* observations of PG 1448+273 in 2017 caught the AGN in a low flux state and where the iron K absorption trough appeared at a much lower centroid

energy of 7.5 keV (Kosec et al. 2020; Laurenti et al. 2021; Reeves et al. 2023) and implying a mean wind velocity of $\approx 0.1c$ (Reeves et al. 2023). In contrast, in the brighter 2022 and 2023 observations, the absorption trough is measured above 9 keV, while all of these later brighter epochs are consistent with the thick disk wind attaining a maximum terminal velocity of $\approx 0.4c$. The higher velocities in the 2022–23 epochs versus 2017 might be connected to the higher X-ray flux in the later observations.

The 2017 epoch of PG 1448+273 may also be unusual, as it occurred during a pronounced X-ray dipping period. This was observed from the *Swift* monitoring during this period (Laurenti et al. 2021), where the X-ray flux dropped by up to an order of magnitude compared to the optical and UV flux. This decrease may have had a substantial effect on the wind properties, with the wind being substantially slower and also of lower ionization. The latter effect is illustrated by the multi-epoch comparison of the RGS spectra (Figure 9, right panel), where a deep trough was present in the 2017 spectrum due O VIII Lyman- α at a velocity of $-0.1c$, as reported in Kosec et al. (2020) and Reeves et al. (2023), but which is absent during the brighter 2022–23 periods. Further monitoring with *XMM-Newton* and *NuSTAR* will help to reveal whether PG 1448+273 continues to maintain the large velocity measured in 2022–23, or whether the AGN wind reacts to any prolonged decreases in luminosity via its ionization and velocity as in the 2017 epoch.

6.3. Kinematics and Wind Driving Mechanisms

Here we estimate the kinematics of the disk wind in PG 1448+273 from the 2023 observations. The mass outflow rates and terminal velocities derived from the disk wind modeling in Section 4.1 (DW thick case) are adopted (Table 2, model (d)). Here, the resultant mass outflow rate (\dot{M}) is expressed in Eddington units. To provide a more conservative estimate of the energetics, the average terminal velocity attained by the wind is adopted (i.e. $v/c = -0.34 \pm 0.02$), rather than the maximum terminal value which is achieved at the innermost edge of the streamline. The kinetic power in Eddington units (\dot{E}) is subsequently:-

$$\dot{E} = \frac{L_{\text{kin}}}{L_{\text{Edd}}} = \frac{1}{\eta}(\gamma - 1)\dot{M} \quad (4)$$

where γ is the Lorentz factor and η is the accretion efficiency (and where $\eta = 0.1$ is adopted here). The corresponding wind momentum thrust in Eddington units is subsequently:-

$$\dot{p} = \frac{\dot{p}_{\text{out}}}{\dot{p}_{\text{Edd}}} = \frac{1}{\eta}\dot{M}\frac{v}{c}. \quad (5)$$

The outflow energetics of PG 1448+273 in 2023 are listed in Table 6, while consistent results are also obtained with the WINE model. Note the absolute values are included in parenthesis, which take into account the uncertainties on the black hole mass measured by Hu et al. (2021). As a result of the large wind velocity and the high mass outflow rate determined by the disk wind modeling, as well as the wide angle nature of the wind, the kinetic power during the 2023 observations reaches about 50% of the Eddington luminosity. This is at least an order of magnitude higher than what is postulated to be significant in terms of mechanical feedback in the host galaxy (Hopkins & Elvis 2010). Furthermore, the normalized momentum rate (compared to Eddington) also ex-

TABLE 6
OUTFLOW ENERGETICS OF PG 1448+273 IN 2023.

Parameter	Value
$< v_{\infty}/c >^a$	-0.34 ± 0.02
\dot{M}^b	$0.84 \pm 0.12 (0.19^{+0.11}_{-0.06} M_{\odot} \text{ yr}^{-1})$
\dot{E}^c	$0.53 \pm 0.09 (6.8^{+4.0}_{-2.4} \times 10^{44} \text{ erg s}^{-1})$
\dot{p}^d	$3.0 \pm 0.5 (1.3^{+0.8}_{-0.5} \times 10^{35} \text{ dyne})$

^a Mean terminal velocity of the wind

^b Mass outflow rate in Eddington units, as per Table 2 (absolute value in parenthesis).

^c Outflow kinetic power in Eddington units.

^d Outflow momentum rate in Eddington units.

ceeds unity, i.e. $\dot{p}_{\text{wind}}/\dot{p}_{\text{Edd}} \approx 3$. In contrast a ratio of about one is predicted for black hole winds, e.g. King & Pounds (2003), arising from the average single electron scattering limit for the radiation field in a moderately Compton thick wind ($N_{\text{H}} \sim 10^{24} \text{ cm}^{-2}$). This is also generally higher than the observed values derived from ultra fast outflow samples, e.g. Tombesi et al. (2013); Gofford et al. (2015).

We also compare the mass outflow rate computed by the diskwind (DW thick case) and WINE models with that obtained by the more simple XSTAR model in Section 4. Here the general form of the mass outflow rate is adopted, according to Tombesi et al. (2013) and Gofford et al. (2015), where:-

$$\dot{M} = 4\pi f_{\text{cov}} \mu m_{\text{p}} N_{\text{H}} v_{\text{out}} R. \quad (6)$$

Here μm_{p} is the average baryonic particle mass ($\mu = 1.27$ for cosmic abundances) and f_{cov} is the geometrical covering, while $N_{\text{H}} = 6.2^{+1.5}_{-2.1} \times 10^{23} \text{ cm}^{-2}$ and $v/c = -0.34 \pm 0.02$ from the XSTAR fits. A covering of $f_{\text{cov}} = 0.7$ is adopted to provide a like for like comparison with the WINE model, while likewise a launch radius of $R = 16R_{\text{S}}$ is used. For these values, then subsequently $\dot{M}_{\text{out}} = 0.09 \pm 0.03 M_{\odot} \text{ yr}^{-1}$, or equivalently $\dot{M}_{\text{out}}/\dot{M}_{\text{Edd}} = 0.40 \pm 0.12$ (for $\eta = 0.1$). The latter value is similar to, but somewhat lower than the values computed by the diskwind model (Table 2, DW Thick case) and WINE (Table 3). On the other hand, the XSTAR value may be somewhat underestimated, as it does not account for special relativistic effects and the de-boosting of the continuum as seen by the wind, as is calculated in Luminari et al. (2020).

Overall it may be difficult to accelerate and sustain such a fast powerful wind by continuum (i.e. Thomson) radiation pressure alone, even for an Eddington limited AGN. The maximum possible wind velocity in the radiative case will also be limited by special relativistic effects. Here, the ability of radiation alone to drive a wind velocity as high as $-0.4c$ will be further restricted, due to the non-negligible de-boosting of the radiation field as received by the outflowing gas (Luminari et al. 2020, 2021).

In contrast, magneto hydrodynamical (or MHD) winds are not limited by such effects and potentially can drive iron K winds from the innermost accretion disk to velocities as high as $-0.6c$ (Fukumura et al. 2010). As illustrated in Figure 3 in Fukumura et al. (2010), the most favorable conditions occur in AGN with steep X-ray spectra (either in α_{ox} or Γ). The relative paucity of hard X-ray photons then prevents over ionization of either Fe XXV or Fe XXVI in the innermost wind regions, where the fastest part of the wind is launched. Such models are able to reproduce the fast wind in PDS 456, attaining a maximum wind velocity of up to $-0.39c$ in that case

(Fukumura et al. 2018). The large velocity width of the absorption profile in PG 1448+273 is reminiscent of the profiles predicted by MHD winds, especially for steep Γ sources due to the more favorable ionization conditions (Fukumura et al. 2018, 2022). This is as a result of the large range in radii over which the wind is launched on the disk, where $v_\infty \propto R^{-1/2}$. In both the MHD and radiation cases (Matzeu et al. 2022), a high accretion rate with respect to Eddington is also beneficial, as this will increase the outflow density, further lowering the wind ionization. Thus in the high accretion rate NLS1s, both the properties of the incident radiation field and MHD processes can play an important part in accelerating and sustaining disk winds to such high velocities.

However the large outflow rates may be at least in part mitigated by a lower geometrical covering of the gas. The broad emission component determines the overall extent of the wind. However if part of the emission profile is formed by a relativistic accretion disk line, e.g. see Parker et al. (2022) or Middei et al. (2023), then the restrictions on the covering fraction could be relaxed. This would help to reconcile the derived mass outflow rate with UV line driven wind simulations. For example in Nomura et al. (2020), the mass outflow rates can approach 50% of Eddington as the Eddington limit is reached; such rates are largely consistent with what is observed here. As demonstrated by Mizumoto et al. (2021), UV line driven winds can be inhomogeneous and produce a wide range in observed outflow velocities as a result of the

in situ acceleration of the wind. The strong UV to soft X-ray excesses in NLS1s such as PG 1448+273, in contrast to AGN with higher masses and low Eddington ratios, may also enhance a line driven wind. Furthermore, in the mildly super Eddington regime, powerful, yet clumpy winds can even be formed by continuum (i.e. Thomson) radiation pressure alone Takeuchi et al. (2013). The properties of these winds, whether they are clumpy and/or inhomogeneous, will be soon revealed by the *Resolve* calorimeter on *XRISM* (Tashiro et al. 2020), which thanks to its high spectral resolution will accurately probe the velocity field of the outflowing gas.

7. ACKNOWLEDGEMENTS

JR and VB acknowledge financial support through NASA grants 80NSSC22K0474 and 80NSSC23K1467. D.P acknowledges financial support from the CNES french spatial agency. A. Luminari acknowledges support from the HORIZON-20 grant “Integrated Activities for the High Energy Astrophysics Domain” (AHEAD-2020), G.A. 871158). SH acknowledges support from the Science and Technologies Facilities Council (STFC) through the studentship grant ST/V506643/1. Based on observations obtained with *XMM-Newton*, an ESA science mission with instruments and contributions directly funded by ESA Member States and NASA and from the *NuSTAR* mission, a project led by the California Institute of Technology, managed by the Jet Propulsion Laboratory, and funded by NASA

REFERENCES

- Bianchi, S., Guainazzi, M., Matt, G., et al. 2007, *A&A*, 467, L19.
 Boroson, T. A. 2002, *ApJ*, 565, 78
 Braitto, V., Reeves, J. N., Severgnini, P., et al. 2021, *MNRAS*, 500, 291
 Braitto, V., Reeves, J. N., Matzeu, G., et al. 2022, *ApJ*, 926, 219.
 Burrows, D. N., Hill, J. E., Nousek, J. A., et al. 2005, *Space Sci. Rev.*, 120, 165.
 Chartas, G., Brandt, W. N., Gallagher, S. C., & Garmire, G. P. 2002, *ApJ*, 579, 169
 Chartas, G. & Canas, M. H. 2018, *ApJ*, 867, 103
 Chartas, G., Cappi, M., Vignali, C., et al. 2021, *ApJ*, 920, 24.
 den Herder, J. W., Brinkman, A. C., Kahn, S. M., et al. 2001, *A&A*, 365, L7
 Di Matteo, T., Springel, V., & Hernquist, L. 2005, *Nature*, 433, 604
 Fabian, A. C., 1999, *MNRAS*, 308, L39
 Faucher-Giguère, C.-A. & Quataert, E. 2012, *MNRAS*, 425, 605
 Fukumura, K., Kazanas, D., Contopoulos, I., et al. 2010, *ApJ*, 723, L228.
 Fukumura, K., Kazanas, D., Shrader, C., et al. 2018, *ApJ*, 864, L27
 Fukumura, K., Dadina, M., Matzeu, G., et al. 2022, *ApJ*, 940, 6.
 Giustini, M. & Proga, D. 2019, *A&A*, 630, A94
 Giustini, M., Rodríguez Hidalgo, P., Reeves, J. N., et al. 2023, *A&A*, 679, A73
 Gofford J., Reeves J. N., Tombesi F., et al., 2013, *MNRAS*, 430, 60
 Gofford, J., Reeves, J. N., McLaughlin, D. E., et al. 2015, *MNRAS*, 451, 4169
 Grupe, D., Wills, B. J., Leighly, K. M., et al. 2004, *AJ*, 127, 156.
 Hagino, K., Odaka, H., Done, C., et al. 2016, *MNRAS*, 461, 3954
 Harrison, F. A., Craig, W. W., Christensen, F. E., et al. 2013, *ApJ*, 770, 103
 Hopkins P. F., Elvis M., 2010, *MNRAS*, 401, 7
 Hu, C., Li, S.-S., Yang, S., et al. 2021, *ApJS*, 253, 20.
 Igo, Z., Parker, M. L., Matzeu, G. A., et al. 2020, *MNRAS*, 493, 1088.
 Iwasawa, K. & Taniguchi, Y. 1993, *ApJ*, 413, L15.
 Jansen, F., Lumb, D., Altieri, B., et al. 2001, *A&A*, 365, L1
 Jiang, J., Walton, D. J., Parker, M. L., et al. 2018, *MNRAS*, 481, 639
 Kalberla, P. M. W., Burton, W. B., Hartmann, D., et al. 2005, *A&A*, 440, 775
 Kallman, T. R., Palmeri, P., Bautista, M. A., Mendoza, C., & Krolik, J. H., 2004, *ApJS*, 155, 675
 King, A. R., 2003, *ApJ*, 596, L27
 King, A. R. & Pounds, K. A. 2003, *MNRAS*, 345, 657
 Kosec, P., Buisson, D. J. K., Parker, M. L., et al. 2018, *MNRAS*, 481, 947
 Kosec, P., Zoghbi, A., Walton, D. J., et al. 2020, *MNRAS*, 495, 4769.
 Lanzuisi, G., Matzeu, G., Baldini, P., et al. 2024, *A&A*, submitted
 Laurenti, M., Luminari, A., Tombesi, F., et al. 2021, *A&A*, 645, A118.
 Longinotti, A. L., Krongold, Y., Guainazzi, M., et al. 2015, *ApJ*, 813, L39
 Luminari, A., Piconcelli, E., Tombesi, F., et al. 2018, *A&A*, 619, A149
 Luminari, A., Tombesi, F., Piconcelli, E., et al. 2020, *A&A*, 633, A55.
 Luminari, A., Nicastro, F., Elvis, M., et al. 2021, *A&A*, 646, A111
 Luminari, A., Marinucci, A., Bianchi, S., et al. 2023, *ApJ*, 950, 160
 Luminari, A., Piconcelli, E., Tombesi, F., et al. 2024, *A&A*, submitted
 Matzeu, G. A., Reeves, J. N., Braitto, V., et al. 2017, *MNRAS*, 472, L15
 Matzeu, G. A., Lieu, M., Costa, M. T., et al. 2022, *MNRAS*, 515, 6172
 Matzeu, G. A., Brusa, M., Lanzuisi, G., et al. 2023, *A&A*, 670, A182
 Middei, R., Nardini, E., Matzeu, G. A., et al. 2023, *A&A*, 680, A50.
 Mizumoto, M., Nomura, M., Done, C., et al. 2021, *MNRAS*, 503, 1442
 Nardini, E., Reeves, J. N., Gofford, J., et al. 2015, *Science*, 347, 860
 Mizumoto, M., Ohsuga, K., & Done, C. 2020, *MNRAS*, 494, 3616.
 Osterbrock, D. E. & Pogge, R. W. 1985, *ApJ*, 297, 166.
 Parker, M. L., Matzeu, G. A., Matthews, J. H., et al. 2022, *MNRAS*, 513, 551
 Parker, M. L., Alston, W. N., Buisson, D. J. K., et al. 2017, *MNRAS*, 469, 1553
 Pinto, C., Alston, W., Parker, M. L., et al. 2018, *MNRAS*, 476, 1021
 Pounds, K. A., Reeves, J. N., King, A. R., et al. 2003, *MNRAS*, 345, 705
 Pounds, K. A. & Vaughan, S. 2012, *MNRAS*, 423, 165.
 Proga, D. & Kallman, T. R. 2004, *ApJ*, 616, 688.
 Rakshit, S., Stalin, C. S., & Kotilainen, J. 2020, *ApJS*, 249, 17.
 Reeves, J. N., O’Brien, P. T., & Ward, M. J. 2003, *ApJ*, 593, L65
 Reeves, J. N., Braitto, V., Gofford, J., et al. 2014, *ApJ*, 780, 45
 Reeves, J. N., Braitto, V., Nardini, E., et al. 2018, *ApJ*, 854, L8.
 Reeves, J. N. & Braitto, V. 2019, *ApJ*, 884, 80
 Reeves, J. N., Braitto, V., Porquet, D., et al. 2023, *ApJ*, 952, 52
 Saez, C., & Chartas, G. 2011, *ApJ*, 737, 91
 Schmidt, M., & Green, R. F. 1983, *ApJ*, 269, 352
 Silk, J., & Rees, M. J., 1998, *A&A*, 331, L1
 Sim, S. A., Long, K.S., Miller, L., & Turner, T.J., 2008, *MNRAS*, 388, 611
 Sim, S. A., Miller, L., Long, K. S., Turner, T. J., & Reeves, J. N. 2010, *MNRAS*, 404, 1369
 Sim S. A., Proga D., Miller L., Long K. S., Turner T. J., 2010, *MNRAS*, 408, 1396
 Strüder, L., Briel, U., Dennerl, K., et al. 2001, *A&A*, 365, L18.
 Takeuchi, S., Ohsuga, K., & Mineshige, S. 2013, *PASJ*, 65, 88.
 Tashiro, M., Maejima, H., Toda, K., et al. 2020, *Proc. SPIE*, 11444, 1144422
 Titarchuk, L. 1994, *ApJ*, 434, 570
 Tombesi, F., Cappi, M., Reeves, J. N., et al. 2010, *A&A*, 521, A57

Tombesi, F., Cappi, M., Reeves, J. N., et al. 2013, MNRAS, 430, 1102
Tombesi, F., Meléndez, M., Veilleux, S., et al. 2015, Nature, 519, 436.
Turner, M. J. L., Abbey, A., Arnaud, M., et al. 2001, A&A, 365, L27

Wilms, J., Allen, A., & McCray, R. 2000, ApJ, 542, 914